Yan, Dongni; Mikkola, Tommi; Lakshmynarayanana, Puramharikrishnan; Tödler, Simon; Schellin, Thomas E.; Neugebauer, Jens; el Moctar, Ould; Hirdaris, Spyros

A study into the FSI modelling of flat plate water entry and related uncertainties

Published in:
Marine Structures

DOI:
10.1016/j.marstruc.2022.103296

Published: 01/11/2022

Document Version
Publisher's PDF, also known as Version of record

Please cite the original version:
Yan, D., Mikkola, T., Lakshmynarayanana, P., Tödler, S., Schellin, T. E., Neugebauer, J., el Moctar, O., & Hirdaris, S. (2022). A study into the FSI modelling of flat plate water entry and related uncertainties. *Marine Structures*, *86*, Article 103296. https://doi.org/10.1016/j.marstruc.2022.103296

Marine Structures 86 (2022) 103296

Contents lists available at ScienceDirect

Marine Structures

journal homepage: www.elsevier.com/locate/marstruc

A study into the FSI modelling of flat plate water entry and related uncertainties

Dongni Yan [a], Tommi Mikkola [a], Arun Lakshmynarayanana [a], Simon Tödter [b], Thomas E. Schellin [b], Jens Neugebauer [b], Ould el Moctar [b], Spyros Hirdaris [a,*]

[a] *Marine Technology Group, Department of Mechanical Engineering, Aalto University, 02150, Espoo, Finland*
[b] *Institute of Ship Technology, Ocean Engineering and Transport Systems (ISMT), University of Duisburg-Essen, 47057, Duisburg, Germany*

ARTICLE INFO

Keywords:
Flat water entry
Impact loads
Fluid structure interactions (FSI)
Uncertainties

ABSTRACT

This paper presents systematic comparisons of experiments against fluid structure interaction (FSI) simulations for flat water plate entry. Special focus is attributed on hydroelasticity and air trapping effects, quantification of the experimental and numerical uncertainties and the validity of modelling assumptions for the prediction of bottom slamming induced loads. Consequently, the American society of Mechanical Engineers standard for Verification and Validation is used to estimate the errors. Numerical and experimental results agree favourably. It is shown that pressures and strains may be prone to spatial effects that lead to minor deviations between experiments and simulations. High frequency vibration modes and model boundary conditions may also influence the results.

1. Introduction

In rough seas, ocean going ships are subject to impact-induced loads that may induce vibrations, noise and affect structural integrity especially in way of the ship bow and stern areas. The same problem is practically relevant to the dynamics of high-speed vessels that may be prone to bow or bottom slamming induced loads.

Early research on the subject was initiated by Von Kármán [1] who applied momentum theory to analytically estimate the magnitude of water impact pressure forces on 2D rigid seaplane floats during landing. Wagner [2] further developed the water impact theory considering water pile-up effects and proposed an asymptotic solution for water entry with small local dead-rise angles. Chuang [3] experimentally explored the influence of impact loads for small deadrise angles and over the years of detailed research on flat water impact investigations [4–14] lead to the conclusion that air trapping and compressibility may also affect local slamming loads. Research by Lwanowski et al. [15], Iafrati and Korobkin [16] and Jiang et al. [17] shed more light into the cushioned impact process. In addition, Huera - Huarte et al. [18] demonstrated that for small angles of impingement the magnitude of impact loads is influenced by damping.

According to Bereznitski [19] an impact is hydroelastic if the period of the first oscillation that occurs after the peak equals twice the period of the peak itself. Faltinsen [20] confirms that hydroelasticity becomes prominent with increasing impact velocities and decreasing impact angles. Impact velocities may then become prone to scale effects associated with surface tension [21]. A review on the role of air cavities by Young et al. [22] indicated that FSI may lead to a lock-in effect between the structural response and flow

* Corresponding author.
E-mail address: spyros.hirdaris@aalto.fi (S. Hirdaris).

https://doi.org/10.1016/j.marstruc.2022.103296
Received 30 July 2021; Received in revised form 24 August 2022; Accepted 27 August 2022
Available online 15 September 2022

induced cavities. The phenomenon has been confirmed by Tödter et al. [6] who also illustrated that after impact, the structure and cavities oscillate at the same frequency. The experimental work of Faltinsen [23] on the variation of the vapour pressure of water in the wake of an impact demonstrated that hydroelastic slamming may also cause cavitation leading to reduced added mass and hence lower structural periods of oscillation.

To date, various authors reviewed the state of the art in modelling local hydroelastic slamming by experiments, analytical models and advanced simulation methods and key publications include [24–28]. Numerous experimental studies on the impact of hydroelasticity on wedge-shaped structures with relatively small deadrise angles were carried out (e.g. Refs. [29–36]). Notwithstanding this, conclusive studies of the effects of flat impact on response are limited. For example, the studies of Okada and Sumi [37] and Mai et al. [38] demonstrate that elastic plates entering the water at angles between 0 and 4 deg experience higher loads due to damping. This phenomenon has been confirmed by Yan et al. [39,40] who measured pressures during hydroelastic drop tests at 0 deg and Shin et al. [41] who carried out drop tests of large flexible flat plates subject to plastic deformation.

Examples of analytical solutions for the prediction of the local hydroelastic slamming loads are presented by Refs. [42–52]. Zhu et al. [42] proposes a formula that makes use of Lagrangean dynamics and the modal superposition method. Faltinsen et al. [46] studied theoretically hydroelastic slamming by representing the structure as an Euler–Bernoulli beam and solving the fluid flow with a velocity potential. This method has been extended by Wang et al. [51] to include the effects of ship forward speed and compression force on the plate structure. Korobkin [47] and Khabakhpasheva [48] analysed the wave impact on elastic plates by combing Wagner theory and Euler–Bernoulli beam theory. Lv and Grenestedt [52] analytically investigated the responses of ship hull bottom panels under slamming loads via a linear elastic Euler-Bernoulli theory. This work demonstrated that (i) the fundamental natural frequency of the hull bottom panel plays a key role in the structural response and (ii) the effect of shear deformation on higher modes of vibration may be significant.

In terms of advanced simulation methods of hydroelastic slamming modelling, different solvers have been implemented in literature. The potential use of Arbitrary Lagrangean-Eulerian (ALE) method and its derivatives has been explored by Refs. [53–60], and the quantification of uncertainties associated with the use of this method for the prediction of local slamming loads are discussed by Wang et al. [61]. Recently FSI models tend to combine meshless computational fluid dynamic (CFD) and simplified applied mechanics methods (e.g., [51,62–68]). For example, Yang and Qui [66] modelled the impact of a rigid flat plates using a constrained interpolation profile (CPI) method to solve the Navier-Stoke equations. Wang and Guedes Soares [67] simulated the impact of an elastic flat plate using Wagner theory and Euler beam models [51,68]. Panciroli et al. ([62–65]), explored the validity of particle methods by comparing numerical results with experimental measurements for the case of the water impact of a flexible wedge. In Ref. [65] they present an FSI model that couples finite element method (FEM) with smoothed particle hydrodynamics (SPH) embedded in the commercial solver LS-DYNA. Parametric studies account for the influence of varying thickness, deadrise angle and impact velocity on dynamic response and show that flexible mode shapes can dominate the structural deformation for hydroelastic impacts. Yet, the range of validity of the SPH method for use in hydroelasticity is limited by the fact that LS-DYNA does not account for the influence of air entrapment and associated ventilation or cavitation effects on dynamics. Recent studies on advanced particle methods (e.g. Refs. [69–76]) suggest that understanding the underlying physics is still under development and therefore quantification of uncertainties remains a medium to long term objective.

Advanced FSI models combing strong coupling between FVM based CFD and FEA have been developed but yet broadly applied to solve local hyderelatic slamming problems. A preliminary study on the assessment of local slamming loads on rigid wedge structures using Reynolds Averaged Navier Stokes Computational Fluid Dynamics (RANS CFD) is presented by Southall et al. [77]. This paper presents a computational procedure for the prediction of pressures, local and global forces for the bow section of a container ship using OpenFOAM and Star-CCM + solvers. The influence of hydrodynamic assumptions on dynamic response is justified by comparisons between experiments and differing numerical strategies of meshing and time-stepping. Partly validated one way coupled FSI methods that utilise both RANS CFD and FEA solvers for the assessment of local slamming loads on flexible wedges are presented by Maki et al. [78,79] and Ren et al. [80]. Whereas the CFD based solutions presented in this method is satisfactory, recent studies by Lakshmynarayanana and Hirdaris [81] and Yan et al. [82] demonstrate that two-way FSI coupling using partitioned methods should be suitably considered for global and local slamming induced loads. The benchmark recently presented by Truong et al. [28] demonstrates that CFD/FEA based FSI methods can be used for the prediction of local ship slamming loads provided that the verification and validation uncertainties are well understood and quantified. This has also been confirmed in the uncertainty quantification study on the use of ALE methods for the prediction of local slamming loads recently presented by Wang et al. [61].

This paper presents systematic comparisons of water entry experiments against fluid structure interaction (FSI) simulations. Special focus is attributed on hydroelasticity and air trapping effects and the validity of modelling assumptions for the prediction of bottom slamming induced loads. In terms of experimental uncertainty both the accuracy of the sensors and the standard deviation of the repetitions is considered, and thirty repetitions are used to reduce the experimental uncertainty. Numerical uncertainty associated with the discretisation is quantified by the Grid Convergence Index (GCI). Consequently, the American society of Mechanical Engineers (ASME) standard for Verification and Validation (V&V) [83] is used to estimate the errors of experiments and simulations.

The remaining of the paper is organized as follows: Section 2 describes the experimental method and test cases. Section 3 illustrates numerical modelling approach and simulation set up. Section 4 compares and discusses the results from simulations and experiments. Section 5 discusses related uncertainties and Section 6 presents conclusions.

2. Experimental method and test case description

The test setup consisted of a vertically moving platform powered by an electric motor, allowing freely adjustable platform velocities and accelerations (see Fig. 1). The platform was positioned above the test section of a circulating water channel of 6.0 m length and 1.5 m width with the water depth set at 0.55 m. A control loop kept the velocity of the test body constant during water impacts.

The elastic test body was modularly built to allow for the assessment of different plate thicknesses and materials. The body's walls and flanges consisted of rigid aluminium plates. The quadratic flat bottom plate of 0.09 m^2 area had a thickness of 4.7 mm and was made of polyoxymethylene copolymers (POM-C) having an elasticity modulus of approximately 2.8 GPa. Screws were used to fasten the bottom plate to the body, and these screws were covered with wax to obtain a smooth bottom surface. A tightened sealing ring ensured that all joints were waterproof. The rigid test body had an aluminium bottom plate of 12.0 mm thickness, which was welded to the walls of the test body. The bottom's shape and its area were the same for the elastic and the rigid test cases. Inside the test body, two stiffeners were fastened to the rigid bottom to minimise deformations during impact.

Three pressure sensors and one accelerometer were placed inside both test bodies. Additionally, the elastic bottom was equipped with two strain gauges. Hammering tests and a Fast Fourier Transformation (FFT) analysis of the corresponding strain gauge signals determined the natural frequency of the elastic bottom plate. Here, the lowest natural frequency turned out to be 147.1 Hz in air, 53.0 Hz on the water surface, and 47.1 Hz when submerged. Figs. 1 and 2 depict the sensor arrangement inside the elastic and the rigid test bodies, respectively. These figures also include the bodies' principal dimensions. Table 1 lists associated x-, y- and z-coordinates that specify the positions of pressure sensors, strain gauges and accelerometer in respect to the centre of the pressure sensor's measuring surface, the centre of the bottom surface of the strain gauges, and the centre of the accelerometer bottom.

Three absolute pressure sensors, Kulite XTM-190(M) depicted as P1, P2, and P3 on Fig. 1 were placed along the centre line of the bottom plates. For the elastic bottom plate, small sleeves made of POM-C with a diameter of 10 mm and a total height of 10.92 mm were glued to the bottom plate at the sensor positions to allow the sensor mounting. For the rigid test body, the bottom plate thickness was reduced to 10.92 mm over a circular area of 20 mm diameter at these sensor positions. The sensor's circular measurement area had a diameter of 3.8 mm. The sensors' nominal range measured pressures up to 1.7 bar; however, their overpressure range enabled pressure measurements up to 3.5 bar. As the sensors recorded absolute pressures, the atmospheric pressure had to be subtracted from every measurement. However, measuring the absolute pressure yields to small relative measurement uncertainties because the rated error is 1% of the nominal pressure range. To increase measurement accuracy, a pressure calibration pump having an uncertainty of 0.1% was used to calibrate the pressure sensors. The pressure sensors did not drift during the impact-induced phase transition. Additionally, the sensors were temperature compensated for temperatures between 15 °C and 60 °C.

A PCB 353B34 accelerometer was located a distance of 30 mm from the bodies' walls above the bottom plate to decouple accelerometer measurements from structural responses. This accelerometer was able to measure acceleration peaks up to 50*g*, where *g* is the acceleration of gravity of 9.81 ms^{-2}. Its sensitivity uncertainty was 5.0%. Two HBM 1-XY-93-3/350 strain gauges were mounted along the centre line of the elastic bottom plate at a distance of 100 and 150 mm between bottom plate edges and strain gauge centres, respectively. The strain gauges measured longitudinal and transverse strains of up to 5.0%. Two additional strain gauges (not shown in Fig. 1) were placed at the elastic test bodies' walls to monitor the temperature compensation of strain gauge measurements. The combined measurement uncertainty due to measurement errors and lateral strains was about 0.8%.

The elastic and the rigid test bodies weighed 18.45 and 20.32 kg, respectively, and they were mounted underneath a load cell to measure integral forces acting on the test bodies during water entry. The HBM U3/10 load cell, which measured forces up to 10.0 kN with an uncertainty of **0.2%,** was connected to the platform via an extension (see Tenzer et al. [29]). A Ballupp BTL5-A11-M1000-P-32 type magnetostrictive sensor with an uncertainty of **0.02%** measured the motion of the platform to yield a reproducible resolution of 4.0 μm. The time derivative of the platform's motion determined its velocity.

A HBM QuantumX MX 410 B data acquisition system (DAQ) transformed the analogue data into digital files. This DAQ system had a resolution of 24 bits and an uncertainty of **0.05%** for pressures, strains and force measurements and an uncertainty of **0.03%** for position and acceleration measurements. A sampling rate of 96 kHz was selected. Tenzer et al. [29] showed that this sampling rate is sufficient to adequately capture pressure peaks. Thirty repetitions were carried out for every impact velocity to allow a statistical data

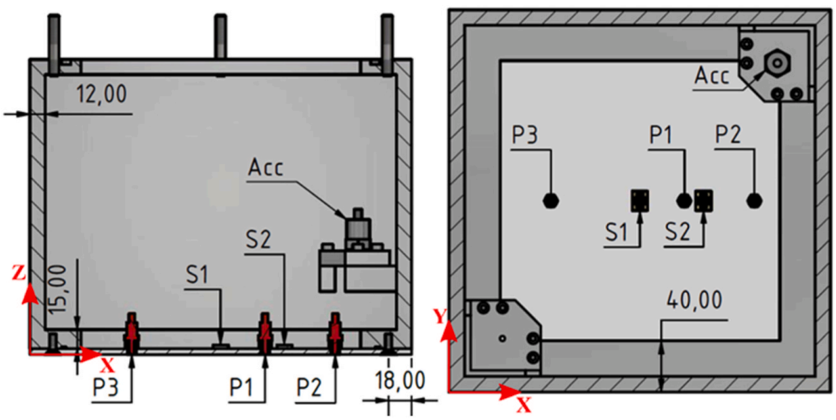

Fig. 1. Side view (left) and top view (right) of the test body with an elastic bottom and the arrangement of sensors P1, P2 and P3, strain gauges S1 and S2 and accelerometer Acc (Displayed values are in mm).

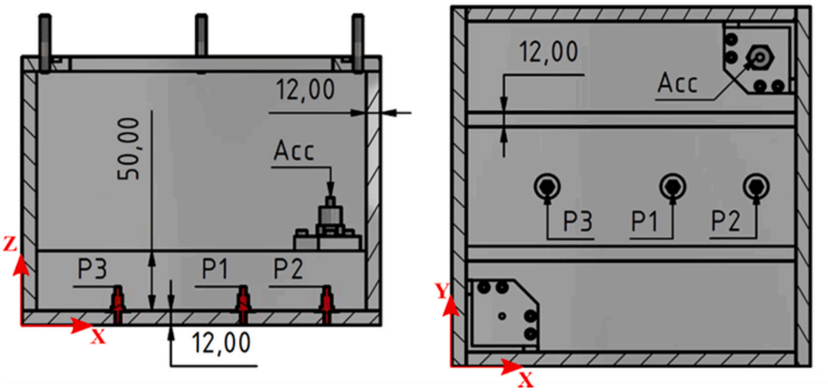

Fig. 2. Side view (left) and top view (right) of the test body with a rigid bottom and the arrangement of sensors P1, P2 and P3 and accelerometer Acc (Displayed values are in mm).

Table 1
Coordinates specifying the positions of the three pressure sensors, the two strain gauges and the accelerometer.

Sensor	X [mm]	Y [mm]	Z [mm]
Pressure Sensor P1	185	150	0.0
Pressure Sensor P2	240[a]/255[b]	150	0.0
Pressure Sensor P3	80	150	0.0
Strain Gauge S1[a]	150	150	4.7
Strain Gauge S2[a]	200	150	4.7
Accelerometer Acc	258	258	74[a]/81.7[b]

[a] Elastic.
[b] Rigid.

evaluation. Table 2 lists the selected impact velocities and accelerations at the beginning of the bodies' motions as well as the actual mean impact velocities of all repetitive impact tests and the associated standard deviations.

3. Numerical methods

In elastic plate slamming, both impact and response are transient and strongly interactive. Thus, the hydroelastic modelling approach presented in this paper followed the two-way FFSI implicit coupling scheme introduced by Lakshmynarayanana and Hirdaris [81]. The dynamic response of the elastic body was idealized using finite elements and was carried out in FEA solver ABAQUS. The fluid domain was idealized by the finite volume (FV) method in which the flow was assumed to be governed by continuity equation and momentum equation following conservation principles (Ferziger and Peric [84]) embedded in STAR CCM+ 13.02 [85]. To enable FFSI using STAR CCM+/ABAQUS interface, impact pressures were mapped to the plate structure and then the structural deformation was transferred back to the fluid solver to update the mesh around plate and in the domain. This FFSI approach was mainly applied for elastic impact, while the corresponding CFD approach with pure fluid domain was used for rigid impact. The main features of fluid and structural idealization methods and solvers used are described in this section by following text.

3.1. Modelling approach

Previous work on slamming by Reddy et al. [86] and Southall et al. [87] has concluded that viscosity has insignificant effects for slamming impacts. Therefore, without considering the viscous effects, the fluid domain was assumed to be governed by continuity equation following mass conservation and Euler equations following momentum conservation. The integral forms of governing equations can be written as:

Continuity Equation:

Table 2
Velocities, standard deviations and accelerations selected for water impact experiments.

Set Velocity [m/s]	Mean Velocity [m/s]	Standard Deviation [m/s]	Acceleration [m/s^2]
0.50	0.519	0.009	0.7
0.75	0.782	0.012	1.1
1.00	1.041	0.013	1.6

$$\frac{\partial}{\partial t}\int_V \rho dV + \oint_A \rho \boldsymbol{v}\cdot d\boldsymbol{a} = 0 \tag{1}$$

Euler equations:

$$\frac{\partial}{\partial t}\int_V \rho \boldsymbol{v} dV + \oint_A \rho \boldsymbol{v}\otimes \mathbf{v}\cdot \mathrm{d}\mathbf{a} = -\oint_A p\boldsymbol{I}\cdot d\boldsymbol{a} + \int_V \boldsymbol{f}_b dV \tag{2}$$

where ρ is the density, $\boldsymbol{v}$ is the continuum velocity, $\otimes$ is the Kronecker product, $\boldsymbol{f}_b$ is the resultant of the body forces (e.g., gravity) per unit volume acting on the continuum, and p is the pressure.

The solution domain was idealized using the Finite Volume (FV) method. Accordingly, the integral form of conservation equations with initial and boundary conditions were applied to the control volumes and discretised into a set of linear algebraic equations. To achieve good convergence, a Gauss-Seidel iterative method and an Algebraic MultiGrid (AMG) preconditioned Biconjugate Gradient Stabilized (BiCGStab) algorithm were selected as the basic iteration scheme and acceleration method, respectively.

Free surface flow effects were implemented by the Volume of Fluid (VOF) surface capturing technique (Hirt and Nichols [88]). To describe the arbitrary free surface interface of two phases (air and water) in the multiphase flow model, the transport equation was solved for a volume fraction namely c, where $c = 0$ and $c = 1$ represent cells that were entirely filled with air and water, respectively.

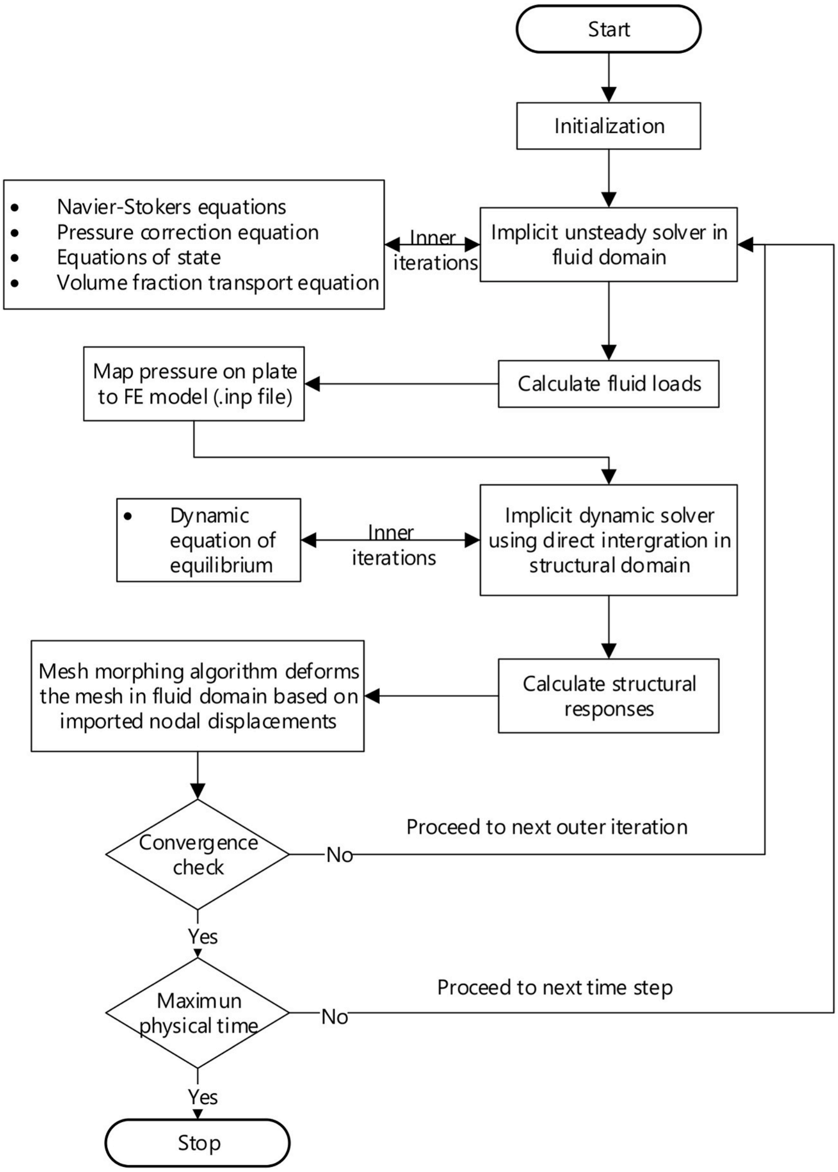

Fig. 3. Flowchart of two-way coupling procedure.

For the study case demonstrated in this paper, simulations captured significant transient variations in the hydrodynamic loads. With the aim to enhance the numerical stability of the solution in two-way coupled simulations water compressibility (STAR CCM+ [85]) was modelled as follows:

$$\rho = \rho_0 + p/c^2 \tag{3}$$

$$\mathrm{d}\rho / \mathrm{d}p = 1/c^2 \tag{4}$$

where ρ is the density, ρ_0 is a density constant, $\mathrm{d}\rho/\mathrm{d}p$ is a derivative of density against pressure and c is the speed of sound in water (1500 m/s).

The dynamic characteristics of the structure under consideration (deformations, stresses, strains, etc.) were evaluated using ABAQUS FEA (Dassault Systèmes [89]). The governing equation for the dynamic response of an elastic body is represented as:

$$M\ddot{x} + C\dot{x} + Kx = F \tag{5}$$

where M, C, K are the mass, damping and stiffness matrices, respectively, F is the external load applied, $\ddot{x}$, $\dot{x}$, x are the acceleration, velocity, and displacement vectors on finite element nodes, respectively.

The modal analysis was carried out in vacuo (i.e., assuming zero damping effects) to calculate the natural frequency of structure where the dynamic equilibrium equation was solved by the Lanczos algorithm. When applying history of loading of slamming pressures, the nonlinear transient dynamic response was calculated using implicit direct integration, where the time integration operators were unconditionally stable for linear systems and there was no mathematical limit on the size of the time increment. The method employs a Hilber-Hughes-Taylor solver which is an extension of the Newmark-β method with controllable numerical damping for time integration (Lakshmynarayanana and Hirdaris [81]; Dassault Systèmes [89]). With inverted operator matrix, the set of simultaneous nonlinear dynamic equilibrium equations were solved at each time increment in an iterative manner using Newton's method. Note that convergence rates obtained using Newton's method have been extensively studied previously and are, therefore, considered satisfactory within the context of this investigation (Dassault Systèmes [89]). As part of this iteration process, the time step sizes used in the fluid domain were set as the limit of the maximum time step size in the structural domain.

The procedure of two-way coupling between fluid domain and structure domain is illustrated in Fig. 3, where the impact pressure is mapped to the plate structure and then the structural deformation is transferred back to the fluid solver to update the mesh around plate and in the domain. The co-simulation ensures that data are exchanged at regular intervals between structural and fluid domains until convergence is reached (STAR CCM+ [85]). The use of implicit coupling schemes is preferred if the mutual dependency on time is high and a small change in one solver will have an immediate effect on the other solver (Lakshmynarayanana and Hirdaris [81]). During elastic plate slamming, hydrodynamic loads and structural deformations were mutually dependent, and their gradients were high. Implicit coupling, therefore, was suitable where both impact and responses were transient and strongly interactive. Even though it was computational costly, it was considered to be more stable as it allowed data exchange more than once per time step (one exchange per every iteration was set in the study).

Throughout the co-simulation process, Star CCM + exported pressure to ABAQUS and imported nodal displacements. Least squares interpolation was used when face-centric source data (fluid pressures) were mapped from fluid cells to structural cells. Shape function interpolation was used when node-centric source data (nodal displacements) were transferred from the FE model to FV cells. The benefit of this mapping process is that a nearly conformal mesh between structural and fluid dynamic solvers is ensured throughout the simulations (STAR CCM+ [85]; Lakshmynarayanana [90]).

For FFSI coupling simulations, the computational time using 40 cores, each running at 2.1 GHz of the Intel Xeon 6230 processors of CSC Finland supercomputing facility, is demonstrated in Table 3. Even if the computational time to run simulations increased, the queue waiting time of using two CPU nodes (20 cores/CPU node) was shorter than using one full CPU node with 40 cores.

3.2. Numerical setup

To develop an accurate and computationally efficient FSI fluid domain for the prediction of slamming forces, some compromises in numerical modelling were necessary. Instead of modelling the exact test tank sizes as described in Section 2, which would make the simulations computationally expensive, the computational domain was assumed to be generally cubic in shape with a length of 1200 mm in both x- and y-directions and with a height of 1000 mm in the z-direction (see Fig. 4).

The plate lower surface was positioned 500 mm above the bottom of the domain. The body volume above the plate was subtracted from the fluid domain, assuming negligible influence due to fluid flow impact. The plate local coordinate system (plate-CSys) was set at

Table 3
Computational time for 0.15s of simulation time.

Velocity [m/s]	Time step [s]	Simulation time [s]	Computational time using one full CPU node with 40 cores [hour]	Computational time using two CPU nodes (20 cores/CPU node) [hour]
0.519	5e-5	0.15	90	130
0.782	4e-5	0.15	113	163
1.041	3e-5	0.15	150	217

the center of the bottom surface. It was assumed that its origin coincides with the global coordinate origin of the fluid domain. Three numerical pressure sensors were located on the plate, based on the experimental sensor locations described in Section 2.

Simulations assumed constant drop velocities; thus, the influence of acceleration of body motion due to gravity was not modelled. Since the approach with moving plate at a constant velocity downwards while keeping the free surface fixed in space was computationally demanding, the plate was fixed in space with the fluid flow moving in the vertical direction upwards with constant velocity (0.519 m/s, 0.782 m/s or 1.041 m/s). This approach avoids grid deformations associated with rigid body motions and facilitates data mapping between fluid and structural solvers (Camilleri [91]). The air-water interface was initialized at 30 mm below the plate bottom surface with the help of a VOF flat wave model at the beginning of the simulation. It benefited the computational cost while making sure that a steady velocity and pressure field was established before impact.

To maintain a sharp interface during impact, High Resolution Interface Capturing (HRIC) discretisation scheme was used along with VOF. This scheme blends upwind and downwind schemes and provides further correction, depending on the local Courant number associated with local flow (Lakshmynarayanana and Hirdaris [81]; Muzaferija et al. [92]). The second-order midpoint rule was employed to evaluate the convective flux surface integral, and a second-order upwind linear interpolation scheme was used to approximate cell face center values. The Hybrid Gauss-LSQ method was utilized to compute the cell gradients. A second-order implicit scheme was selected for temporal discretisation. The Semi-Implicit-Method for Pressure-Linked Equations (SIMPLE) algorithm was employed as the pressure-velocity coupling algorithm to correct pressure and density and satisfy fluid continuity condition. Under-relaxation factors of 0.2 for pressure and 0.8 for velocity and 20 iterations per time step were selected to ensure better convergence of hydrodynamic pressures.

Regarding the boundary conditions, the plate surface and the connected side surfaces were specified as walls; the bottom boundary was specified as velocity inlet; the top boundary was specified as pressure outlet under atmospheric pressure conditions, and all remaining surfaces parallel to the z-axis were assumed symmetrical to reflect the flow locally, both in way of the normal velocity and normal gradients of all variables (see Table 4).

Mesh morphing was applied to move the fluid vertices to conform to the solid surface and to maintain a reasonable quality fluid grid. The morpher first used the control point displacements originating from mesh vertices on morphing boundaries to construct an interpolation field. Then it used the interpolation field to translate the mesh vertices to their new positions. Three kinds of morphing boundaries were used in the fluid domain: (a) co-simulation boundaries for plates where mesh vertices on their surface move according to the imported displacement field, (b) in-plane boundaries for symmetry planes where mesh vertices only moved on the symmetry plane with zero displacement normal to this plane, (c) fixed boundaries for all inlets, outlets, and wall surfaces above the plate with mesh vertices of zero displacement.

Unstructured hexahedral cells based on trimmed Cartesian grids were used to discretise the fluid domain. To capture accurately the free surface and high gradients of pressure and fluid velocities around the plate, volumetric blocks were used to refine mesh zones in the vicinity of the plate and around the free surface. The grid in Fig. 5, henceforth, is referred to as a medium grid. Two additional grids (coarse and fine) were employed later for convergence study in Section 5. According to ASME [93], a minimum grid refinement ratio of 1.3 is considered acceptable to differentiate the discretisation error from other sources of error, such as iterative convergence errors, computer round-off error, etc. Based on this requirement and according to Lakshmynarayanana [90] and Stern et al. [94], a refinement ratio of 2.0 may be too large for industrial CFD purposes. As the ratio of $\sqrt{2}$ was deemed more appropriate for both temporal and spatial refinements, we used this ratio for our case study at the water entry velocity of 0.782 m/s. The time step and FV grid particulars for temporal and spatial discretisation convergence studies are listed in Tables 5 and 6, where the structural grid size is kept consistent for these cases. The resolution factor describes the number of time steps applied to compute the varying impact load over one period of

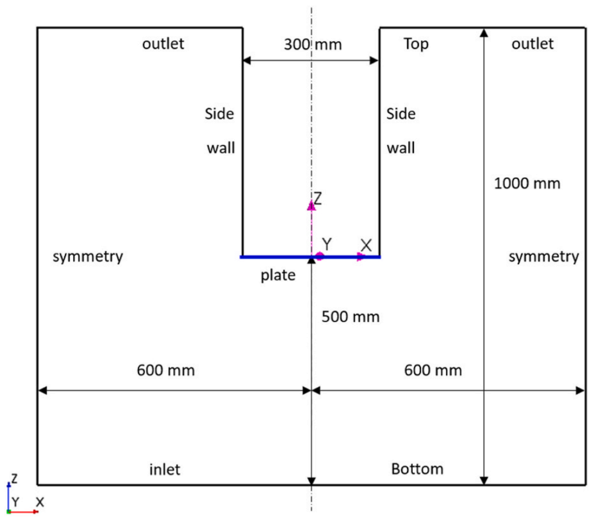

Fig. 4. Fluid domain showing applied boundary condition types and distances towards the boundaries.

Table 4
Boundary conditions in fluid domain.

Boundary surfaces	Boundary conditions
Plate	wall
Side	wall
Bottom	velocity inlet
Top	pressure outlet
Symmetry	symmetry

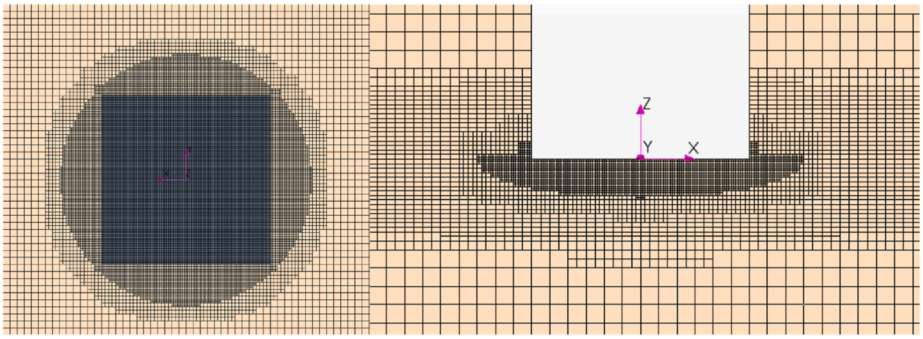

Fig. 5. Mesh discretisation on and around the plate and of the free surface.

elastic case. This value is delimited by the first two crests of variation after impact.

Considering the computational cost and only small advantages of the fine grid, the medium grid was preferred and applied for all water entry velocities, where the plate and surrounding domain were discretised by 3 mm square grids and the fluid domain comprised 570,187 cells in total. The corresponding time step implied both numerical accuracy and stability because (1) their resolution factors are large enough and (2) the maximum courant number is less than 0.5. A resolution factor of 472 for time discretisation of 4e-5s was shown to provide good approximation to the wet frequency of the first flexible mode (i.e., 53 Hz) at a reasonable computational cost. This is also confirmed by the temporal discretisation convergence study discussed in Section 5 for a medium grid. The numerical time steps for all water entry velocity cases are listed in Table 7.

To avoid simulation failure due to topology inconsistency between structural and fluid dynamic models, the origin in the structural domain was located at the geometric center of the plate's bottom surface. Only the elastic plate made of POM was modelled in the structure domain. And it was modelled as a square-shaped section of 300 mm width on the x-y plane and 4.7 mm in-plane thickness along the z-axis. Material assumptions were assumed as orthotropic (i.e., plane stress conditions) with the POM material properties listed in Table 8.

The polyoxymethylene plate structure was discretised by 8-node continuum shell element (SC8R) implemented in ABAQUS FEA library. This element was based on first-order transverse shear flexible theory for which the transverse shear strain was assumed to be constant throughout the thickness of the shell. For a homogeneous shell made of linear and orthotropic elastic material, to calculate the transverse shear stiffness of the section of the shell element, a shear correction factor of the order 5/6 was assumed and applied together with the shear moduli, shell thickness and a dimensionless factor. This dimensionless factor was used to prevent the shear stiffness from becoming too large in thin shells discretised by area elements (Dassault Systèmes [89]).

Camilleri [91] and Xiao and Batra [95] introduced the stiffness proportional Rayleigh damping to account for structural damping when investigating local water slamming loads, which dampens the high frequency components and improves the stability of the solution. Along these lines and suggestions of Dassault Systèmes [89], the stiffness proportional damping factor employed here corresponded to 4% critical damping.

Three different kinds of boundary conditions were applied on the structure (see Fig. 6). Fixed boundary conditions were applied on the vertical lines in way of the 16 vertical screws. These vertical lines were located 18 mm away from the plates' outer edges. Displacements of plate outer edges in x- and y-directions were restricted, but they were free to move in the z-direction. The aluminum flange existed only on top of the plate. Therefore, line locations at one-third of the in-plane distance between the inner edge of the flange and the screws were idealized as pinned constraints restricting the displacements in the x-, y- and z-directions. Eight grams of

Table 5
Time step variation cases.

FV Grid	FV Grid cells	Time step [s]	Resolution Factor
Medium	570,187	2.8e-5	674
Medium	570,187	4.0e-5	472
Medium	570,187	5.7e-5	331

Table 6
FV grid and time step variation cases.

Grid Level	FV grid	FV grid cells	Time step [s]	Resolution Factor
1	Fine	1,507,825	2.8e-5	674
2	Medium	570,187	4.0e-5	472
3	Coarse	239,210	5.7e-5	331

Table 7
Numerical time steps.

Velocity [m/s]	Time step [s]	Resolution Factor	Maximum Courant number
0.519	5e-5	377	0.33
0.782	4e-5	472	0.37
1.041	3e-5	629	0.40

Table 8
POM Material properties.

Properties	Values
Young's modulus	2800 MPa
Poisson's ratio	0.3
Shear modulus	1077 MPa
Density	1410 kg/m^3

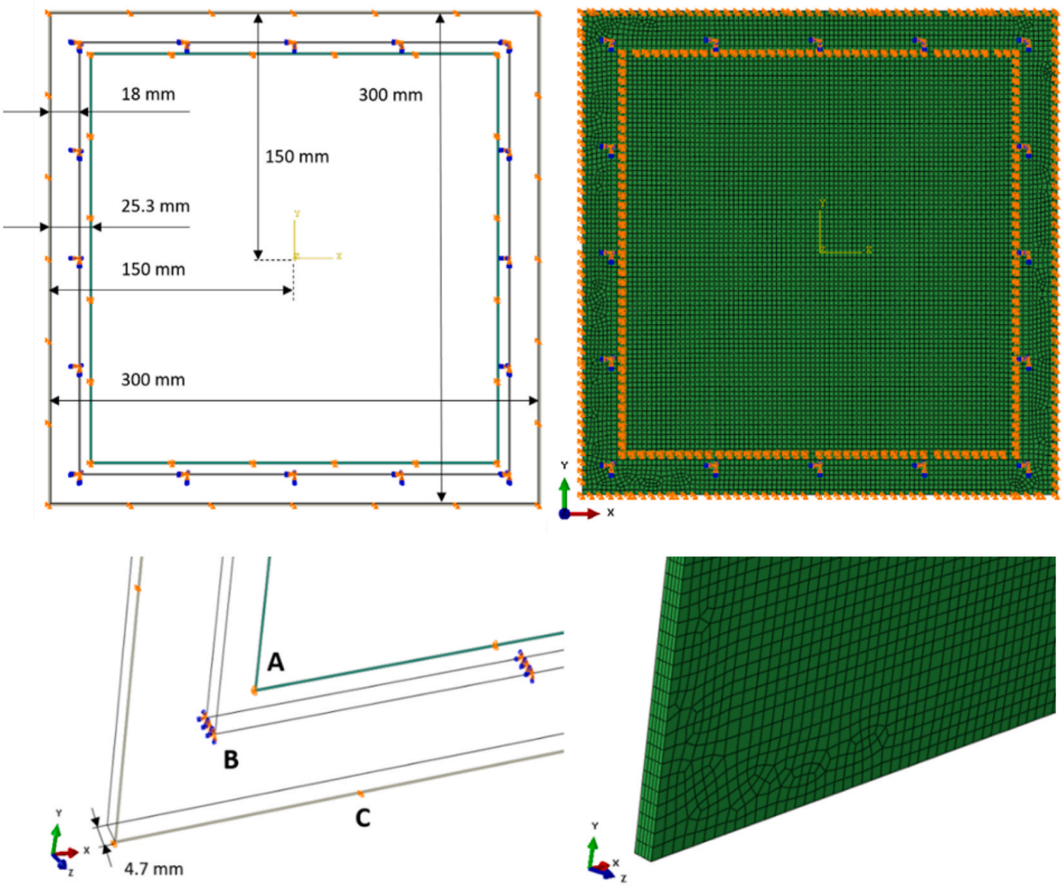

Fig. 6. Three-dimensional plate FE model with 8-node continuum shell elements and structural boundary conditions (A: pinned; B: fixed; C: restricted displacements in x- and y-directions).

point masses were added at each sensor location to idealize local sensors.

According to Stenius et al. [36], for a water entry velocity of 3.5 m/s and a plate modelled as a 500 mm by 500 mm in-plane section size, an element size of 10 mm is needed to obtain sufficient numerical accuracy. However, this must be balanced against computational costs when determining the center deformation of the plate. An element size of only 5 mm would improve the accuracy when modelling strains close to the plate's edge.

As the square-shaped plate studied in this paper was of slightly smaller size and lower impact velocities and strains close to the plate edge were of only minor concern, a mesh of the order of 3 mm was used. This resulted in 50,660 plate elements. Note that this 3 mm structural element size also matched the size of medium fluid grid in way of the FFSI interface. Thus, the discretisation approach presented ensured accuracy of hydro-structural pressure mapping. Five SC8R elements were stacked through shared nodes along the thickness of the plate to provide better refined through-thickness response prediction. A summary of grid and time step particulars are presented in Table 9, where the FE grid refinement ratio is $\sqrt{2}$. Temporal and spatial discretisation convergence studies combining the refinement both in FV and FE grids are discussed in Section 5. These studies confirm that a mesh size of 3 mm suits the medium FV grid.

A modal analysis was used to obtain the fundamental natural frequency of the plate of 148.9 Hz. Although this magnitude exceeded the experimental value of 147.1 Hz, considering modelling uncertainties associated with the tightness of the screws, the additional cable masses on plates and the existence of the top plating, we considered our current numerical structure model to be acceptable. The fundamental natural frequency was sensitive to modelling details; for example, without considering at all the sensors point masses, the difference in frequency would be about 20 Hz. Additionally, the numerical fundamental natural frequency was calculated assuming vacuum conditions, whereas experimental values included the influence of the added mass of air. This also contributed to the deviation between numerical and experimental natural frequencies.

4. Comparison of numerical and experimental results

This section presents comparisons of numerical predictions based on both pure CFD and two-way FFSI simulations against experimental results of Tödter et al. [6]. The analysis focused on comparisons of impact pressures and forces, structural deformations, and air entrapment.

4.1. Comparison of CFD and experimental results for rigid structure

Fig. 7 illustrates comparisons of CFD simulations with experimental data in way of pressure sensor P1 for test cases corresponding to three different impact velocities ((a), (b), (c)). The left graphs show a direct comparison with results from one experimental test, while the right graphs demonstrate the comparison with a band range of 30 repetitive experimental results to indicate the repeatability uncertainty of the experiments. To suitably compare measurements against CFD simulation results, oscillation components after the peak are filtered out by 5th order lowpass filter.

Some initial conclusions were made from the observations. First, the peak values from the CFD simulations were generally slightly larger than experimental peak values. However, these differences between peak values became smaller when comparing CFD results to the band ranges of experimental results. This slightly larger pressure in CFD simulations could be caused by the fact that in pure CFD simulation, no deflection of structure was considered (infinite rigidity of structure), while in the experiments, the aluminum structure was not completely rigid.

Impact force comparisons between CFD simulations and experiments for 0.782 m/s entry velocity are shown in Fig. 8. The same filtering method applied in Fig. 7 is used. Forces rise and decay in the same fashion as pressures. The maximum experimental impact force of band range seems higher than the one predicted by simulation. This could be attributed to uncertainties associated with the entry velocities. As shown in Table 2 in experiments there is slight variation in entry velocities. On the other hand, in simulations we use mean values of measured entry velocities. An investigation of varying entry velocities with $+1\ \sigma$, $+2\ \sigma$ and $+3\ \sigma$ (σ is the standard derivation of entry velocity of 0.782 m/s) is carried out. As shown in the right graph of Fig. 8, the impact forces increase with increasing entry velocity, and get closer to the experimental peak.

4.2. Comparison of FFSI and experimental results for the elastic structure

Fig. 9 illustrates favorable comparisons of FFSI simulations with experimental data in way of pressure sensor P1 for hydroelastic test cases corresponding to three different impact velocities. The numerical records of the lowest entry velocity (0.519 m/s) deviated slightly from experimental data, where the vibration frequency was smaller than that measured in the test tank. From an overall perspective, the pressure results from the simulations were relatively smoother than the experimental results, where small fluctuations were captured. The first fluctuation peak is approximately 50% of the main peak value captured in simulations. This could be

Table 9
FV and FE grid and time step variation cases.

Grid Level	FV grid	FV grid cells	FE grid cells	Time step [s]	Resolution Factor
1	Fine	1,507,825	100,420	2.8e-5	674
2	Medium	570,187	50,660	4.0e-5	472
3	Coarse	239,210	26,885	5.7e-5	331

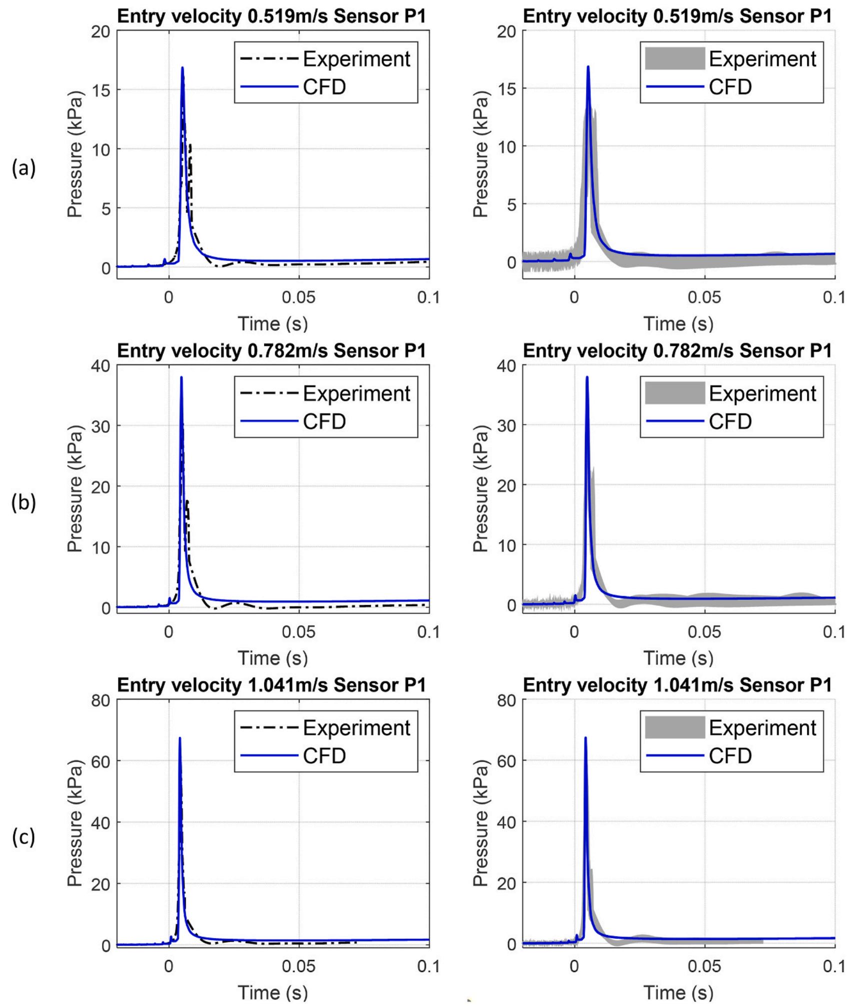

Fig. 7. CFD versus experimental pressures at P1 location for different entry velocities of the rigid plate.

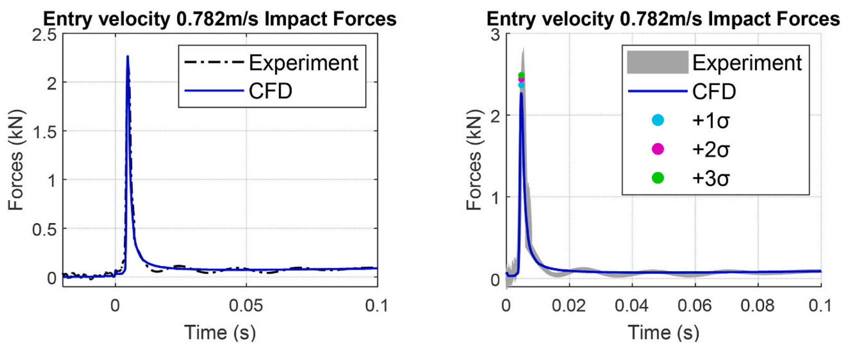

Fig. 8. CFD versus experimental impact force for rigid impacts at entry velocity 0.782 m/s. The graphs display the effect of varying entry velocities with $+1\ \sigma$, $+2\ \sigma$ and $+3\ \sigma$ (σ is the standard derivation of entry velocity of 0.782 m/s).

attributed to the influence of higher order vibration modes, also observed in experiments. In way of the first two crests of numerical and experimental pressure results depicted by sensor P1, differences of pressure amplitudes indicated that the plate vibrated upwards with larger amplitudes in way of water entry. This could be attributed to the fact that the experimental aluminum flange on top of the plate had a broader influencing area and, therefore, provided additional rigidity compared to the FFSI numerical idealization, which was constrained by boundary conditions. The differences between simulation peaks and experiments increases with increasing entry

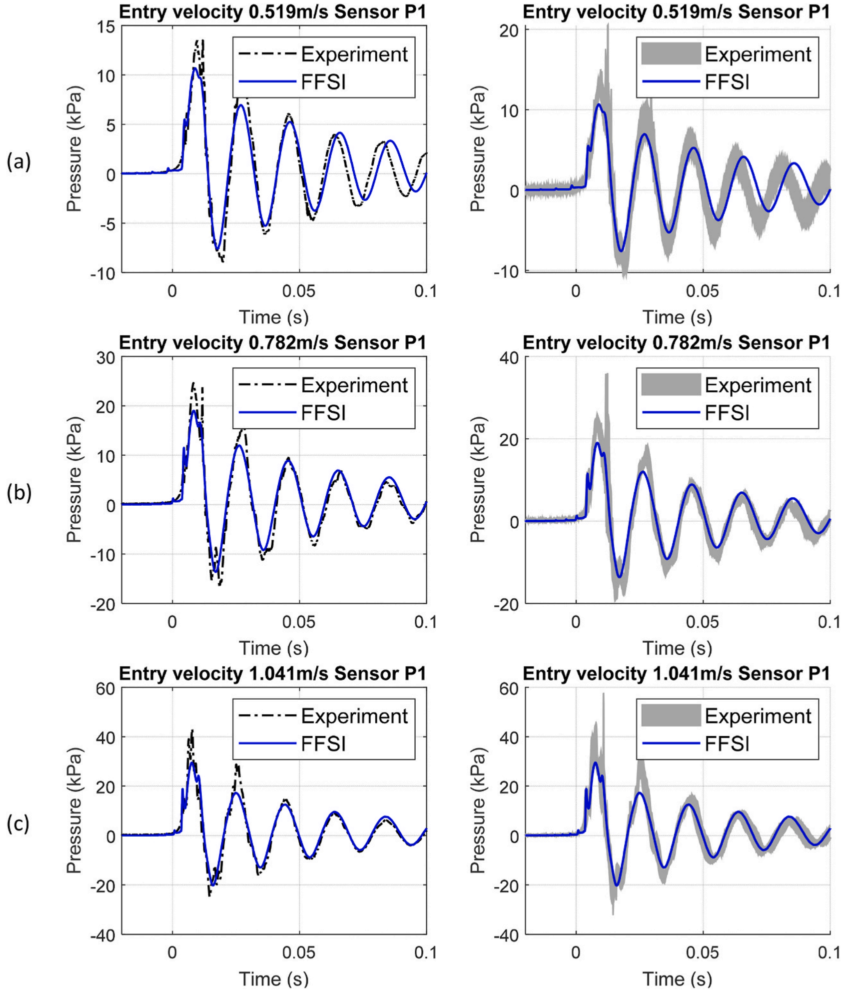

Fig. 9. FFSI pressure versus experimental pressure at P1 location for hydroelastic impacts at different entry velocities.

velocities. This could also be linked to differences in the boundary conditions used in the test rig and simulations. In the experiments, the additional rigidity from the aluminum flange on top of the plate limited the amplitude of upward vibrations. Therefore, the air trapped under the plate during experiments has been lower. When the entry velocity increases, the air trapped under the plate during pressure peak time increases. In any case, the minor differences observed between experimental and computational results decayed as FFSI reached quasi-steady state. When plotting the simulated pressure against the time histories of experimental pressure band of all 30 repetitions at sensor P1 in Fig. 9, except for the previous observed features during comparison, the simulated results generally fell into the range of the experimental results, and the repeatability uncertainties of the measurements were explicitly captured.

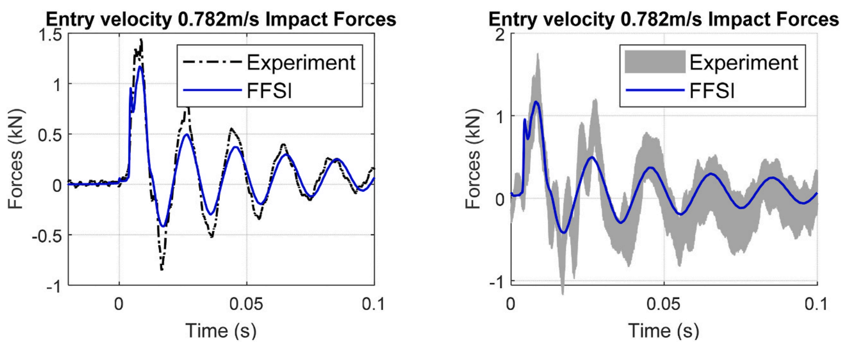

Fig. 10. FFSI impact force vs. experimental impact force for hydroelastic impacts at entry velocity 0.782 m/s.

Fig. 10 compares simulated impact forces against results from one experiment (left) as well as the band of 30 experimental results (right) on the plate for 0.782 m/s entry velocity. At the first, peak differences between test and simulation were within 20%. However, they became more obvious at the succeeding two peaks and converged as signals decayed. This could be attributed to uncertainty associated with the empirical Rayleigh damping factor of 4% that was used to capture the main characteristics of the FFSI plate vibration phenomena (see Section 3.2).

Fig. 11 demonstrate strains in way of two strain gauges namely S1 (at mid plate) and S2 (near plate edge) for water entry velocity 1.041 m/s (see also Fig. 1). Strains at S2 and S1 occurred at similar times when impact initiated. Computational and experimental results matched well for the first two vibration cycles. Note that the vibrations captured during the experiment in way of the first numerical trough were not captured by the numerical model. The second peak captured by S1 (upper right graph of Fig. 11) may be the result of the decreasing reliability of the sensor. Usually strain measurements align with force and pressure trends (see time series of S2). However, they do not capture high-frequency vibrations associated with inertia effects. In the later vibration cycles, the deviation became larger in term of amplitude, as shown in left graphs. However, when comparing to the band of 30 experimental results, the simulated outcomes were within the range of vibration amplitudes, which indicated the FFSI simulation results were reasonable, considering the uncertainties from experiments.

4.3. The influence of air entrapment

Air entrapment during impact was recorded by a high-speed imaging camera during experiments. To better understand the air entrapment process, experiments were compared against simulation results. Special focus was attributed on qualitative comparisons of relevance to the volume fraction of air and its distribution on the plate at different time instances. Air entrapment features idealized by experiments and simulations are directly comparable for cells where air occupies over 50%. Fig. 12 and Fig. 13 show comparisons of results for the rigid and flexible cases with water entry velocity of 1.041 m/s.

In Fig. 12, column A shows experimental results and column B shows results from simulations. Stage (a) represents impact at the start of the water entry when the space under the plate bottom is almost full of air. Stage (b) demonstrates an initial period when the plate enters the water and most air is still trapped at the center of the plate (bright white area in the experiments). Simulation results show similar features, namely (1) the volume fraction of air near the plate central area is nearly 100%, so there is large area of trapped air in way of the plate center; (2) near the plate edge, the volume fraction of air decreases to about 95% as compared to stage (a). It may be concluded that some air is escaping from the central air pockets towards the edge of plate. This phenomenon conveys the influence of fluctuated water near the plate edge as shown in the experimental graph at stage (b). Stage (c) corresponds to the moment after the first pressure peak. The pressure decreases to around 20% of its peak value and the air volume under the plate is decreased. The simulated area of trapped air in way of the plate central area decreases significantly and the average volume fraction of air is around 93%. More air is escaping through the edges while the area of fluctuated water is getting larger. The latter is well shown in both experiments and simulations (dark, bubbly area in the experiments and the color transition from orange to yellow in the simulations). Review of stages (d) and (e) demonstrate that in both experiments and simulations the air under water diminishes gradually as we

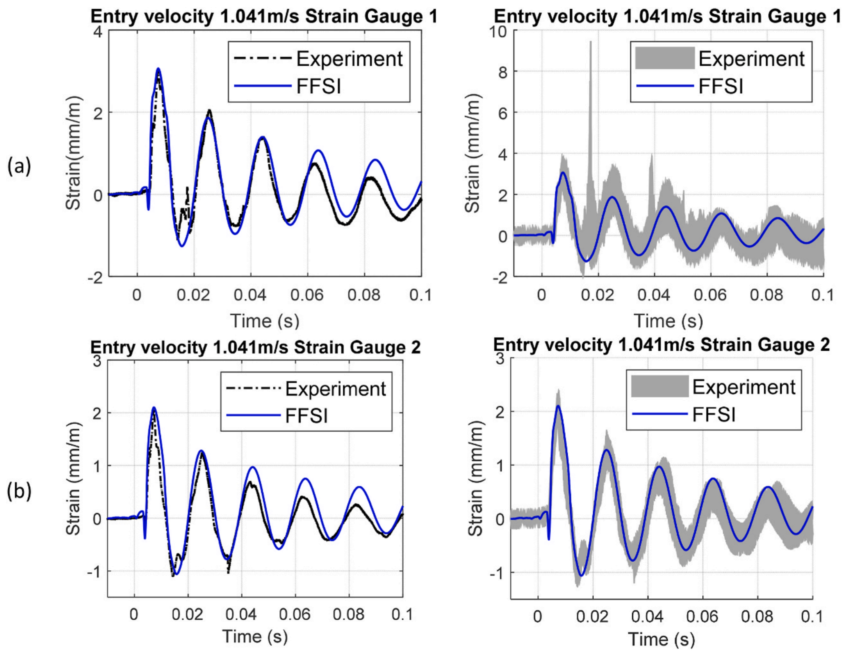

Fig. 11. FFSI vs. experimental strains at (a) S1 and (b) S2 for hydroelastic water entry at a velocity 1.041 m/s.

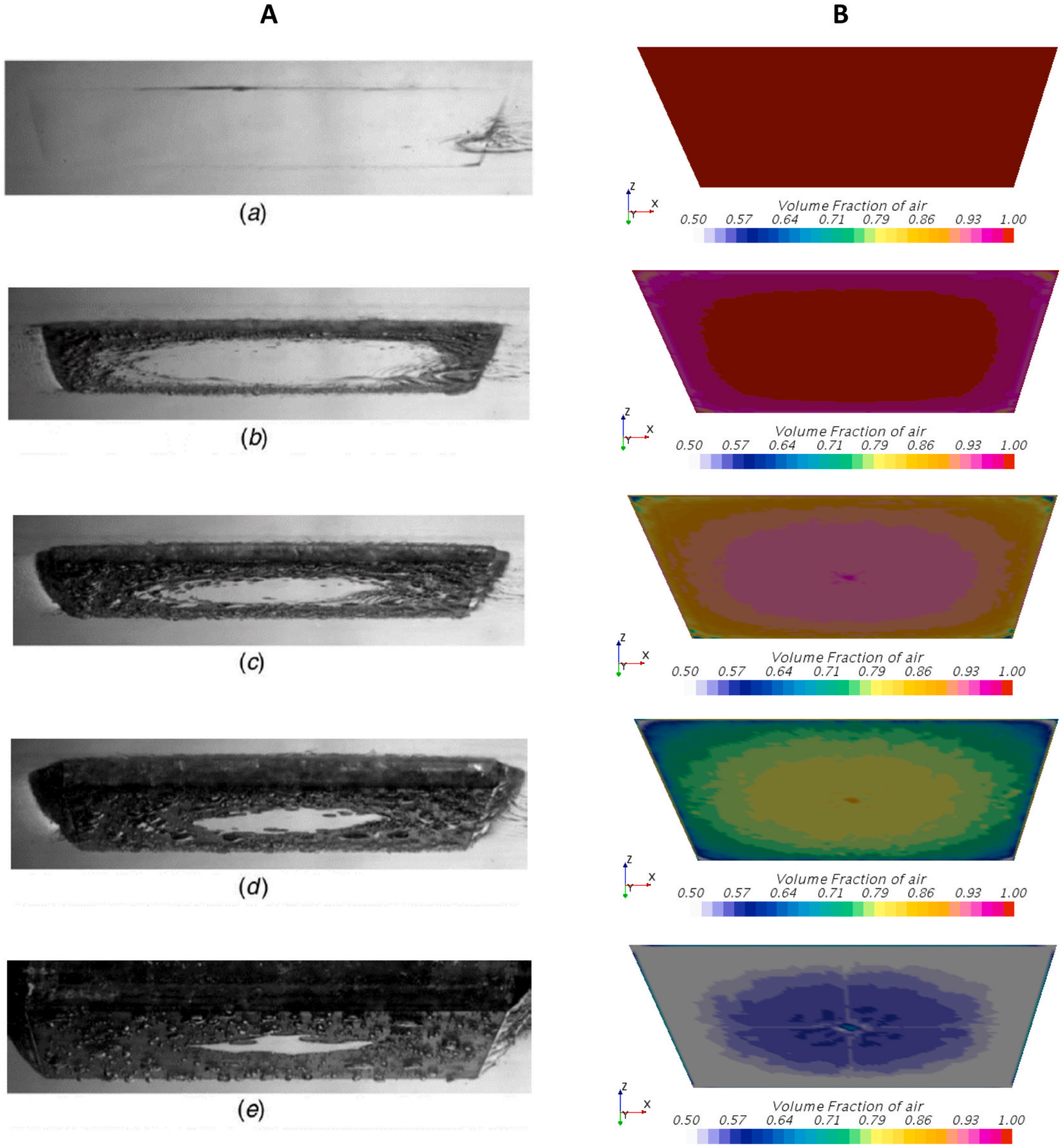

Fig. 12. A: air entrapment underneath the rigid plate bottom at different time instants (t) of the water entry (1.041 m/s) for (a) impact, (b) t = 2.500 ms, (c) t = 5.833 ms, (d) t = 10.832 ms, (e) t = 30.830 ms. B: air entrapment in CFD simulation.

move away from the center of the plate. In simulations the average volume fraction of air near the plate center decreases from about 80% at stage (d) to about 55% at stage (e). Consequently, the percentages of air entrapped in central cells are lower than in stages (b) and (c). It is noted that the simulation method assumed infinite rigidity. In experiments some local deformations in way of the plate center may exist, possibly leading to slightly different levels of air entrapment. However, based on overall comparisons their influence is not that significant.

In Fig. 13 column A and B display the volume of fraction of air from experiments and simulations. Column C displays a version of structural deformations following simulations. Stage (a) represents impact at the start of the water entry when the space under the plate bottom is almost full of air. Stages (b) and (c) demonstrated a gradual process whereby the pressure reaches approximately 70% of its first peak. The maximum structural displacements are 3.4 mm during stage (b) and 3.9 mm during stage (c). The entrapped air is in way of the center area of the deformed plate (white and dark red areas in the experiment and simulations respectively). Stage (d) demonstrates the moment that the plate vibrates vertically from its crest to its neutral position. Stage (e) demonstrates the moment the plate vibrates from the neutral axis to the bottom. At stage (d) the maximum structural displacement is 2.6 mm. During deformation, air is pushed out from the central area and a ring-shaped distribution forms. The phenomenon is observed in both experiments and simulations (see the dark, bubbly ring in the experiment and the dark red ring in the simulations at stage d). The latter observation suggests that the volume fraction of air with average value of 0.9 is distributed partially in the center and partially as a ring shape

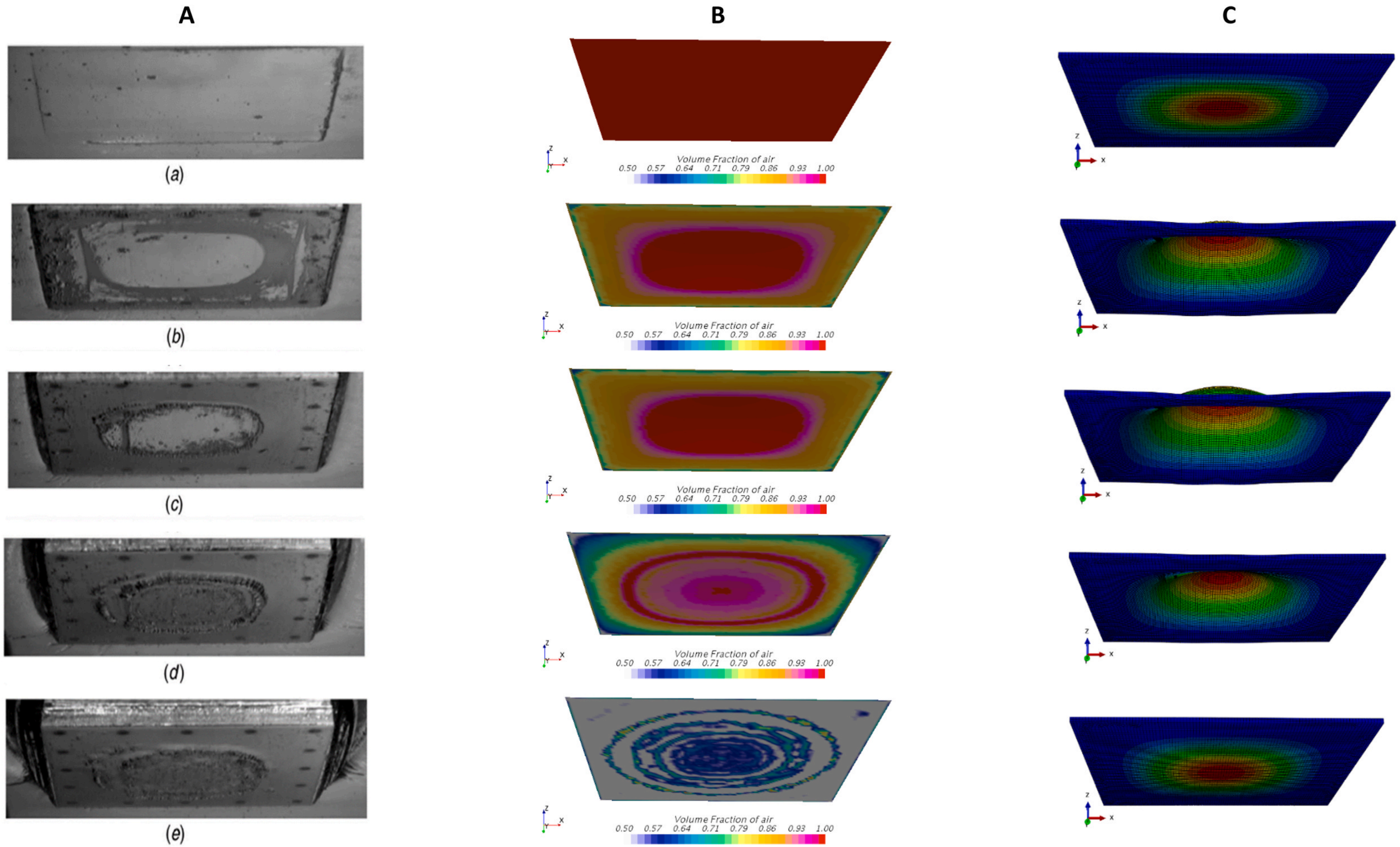

Fig. 13. A: air entrapment underneath the elastic plate bottom at different time instants (t) of water entry (1.041 m/s) for (a) impact, (b) $t = 5.500$ ms, (c) $t = 5.833$ ms, (d) $t = 10.832$ ms, (e) $t = 30.830$ ms. B: air entrapment in FFSI simulation. C: structural displacement with deformation scale factor of 15.

between the plate center and edge. After one vibration cycle, air and water mix and lumpy air bubbles form. The simulated area is slightly wider than the observed in experiments.

5. Discussion of numerical and experimental uncertainties

Experimental uncertainties are important for the validation of numerical methods. Usually, validation involves comparison of numerical and experimental results, estimation of uncertainties, errors, numerical convergence criteria. Experiments may be subject to systematic errors associated with sensor accuracies, repeatability, and reproducibility influences (Smith et al. [96]).

The repeatability of errors of relevance to the study presented in this paper was ensured throughout 30 repetitions in experiments under the same conditions. Reproducibility was neglected as experiments were completed by the same person. The comparisons of the numerical simulations with the experimental results showed generally favorable agreement with regard to temporal coincidences, peak values, and amplitude and frequency of decays after hydroelastic impacts. As numerical uncertainties were quite important to results accuracy and the reliability of experiments was crucial for the suitability evaluation of numerical methods, here the influence of uncertainties from both experimental and numerical aspects are further highlighted below.

Numerical solutions are always approximations and naturally include errors. Systematic errors comprise discretisation errors, modeling errors, iteration errors, and round-off errors. The average iterative errors are often at least one order of magnitude smaller than the grid-spacing and time-step uncertainty (Xing and Stern [97], Huang et al. [98]). Discretisation errors are considered as the dominant source of numerical errors in the computational simulations presented. Iteration uncertainty and round-off error were assumed negligible (Wang et al. [61]).

Spatial and temporal discretisation convergence studies were carried out to assess the sensitivity of the FSI solution to time step size and grid spacing. The solution variables applied were the pressure at P1 and the force on the plate's bottom. The period studied starts from the point where wave loads attain a quarter of their peak value, to the point where they drop back to the same after they reach their peak. Pressure and force impulses were used to represent the momentum transferred from the fluid to the structure. The integrals were approximated using the trapezoidal rule.

The Grid Convergence Index (GCI) method based on the Richardson Extrapolation technique of ASME [93] was applied here to estimate numerical errors and uncertainties. The fine GCI was calculated using the factor of safety $Fs = 1.25$ [99] and a grid refinement factor $r_{21} = \sqrt{2}$ based on the formulae:

$$\mathrm{GCI}^{12} = \frac{Fs \cdot e_a^{12}}{r_{21}^{p} - 1} \tag{6}$$

The approximate relative error e_a^{12} and the observed order of convergence p were calculated as:

$$e_a^{12} = \left| \frac{\varnothing_1 - \varnothing_2}{\varnothing_1} \right| \tag{7}$$

$$p = \frac{1}{\ln(r_{21})} \left| \ln|\varepsilon_{32}/\varepsilon_{21}| \right| \tag{8}$$

Here $\varepsilon_{32} = \varnothing_3 - \varnothing_2$, $\varepsilon_{21} = \varnothing_2 - \varnothing_1$, and $\varnothing_k$ denotes the solution on the kth discretisation (ASME [93]). The resulting quantities are listed in Tables 10–12.

As discussed in Section 3.2, both temporal and spatial discretisation were of the second order as governed by the leading term of the truncation error. However, the existence of boundary conditions, numerical models, grid stretching and quality as well as non-linearities in the solution may lead to lower order of convergence (Roache [100]). A higher observed order of convergence does not necessarily imply greater numerical accuracy. However, the simulated values converge more rapidly (Camilleri [91], Lakshmynarayanana [90]). The orders of convergence shown in Tables 10–12 are within reasonable range compared to the theoretical order. Notably force impulses converge more rapidly than pressure impulse at P1. To reflect numerical uncertainties, the CGI was calculated. The GCI indicates an error band on how far the solution deviates from the asymptotic value and how much the solution varies from solutions obtained on refined grids and time steps (Roache [100]). A factor of safety of 1.25 was used, as three discretisation levels were used and the asymptotic convergence levels were approximately 1.0. This indicated that the computation was within the asymptotic range for both spatial and temporal discretisation and numerical uncertainties associated with the discretisation errors were rather low. It is assumed that a significant contribution to the total uncertainty of the numerical predictions originates from the modelling assumptions and especially related to the boundary condition modelling in the structural domain. It is further observed that the GCI values associated with variation of just the time step in Table 10 are significantly lower than the values for the combined

Table 10
Temporal convergence verification parameters for load impulses (Hydroelastic impact at a velocity of 0.782 m/s).

Verification parameters	Pressure impulse at P1	Force impulse
Observed order of convergence, p	1.72	2.19
GCI^{12}	0.003	0.001
GCI^{23}	0.006	0.002
Asymptotic convergence level, $GCI^{23} / (r^p * GCI^{12})$	1.002	1.001

Table 11
Combined FV grid and temporal convergence verification parameters for load impulses (Hydroelastic impact at a velocity of 0.782 m/s).

Verification parameters	Pressure impulse at P1	Force impulse
Observed order of convergence, p	1.55	2.80
GCI^{12}	0.060	0.013
GCI^{23}	0.106	0.036
Asymptotic convergence level, $GCI^{23} / (r^p * GCI^{12})$	1.04	1.02

Table 12
Combined FV grid, FE grid and temporal convergence verification parameters for load impulses (Hydroelastic impact at a velocity of 0.782 m/s).

Verification parameters	Pressure impulse at P1	Force impulse
Observed order of convergence, p	1.31	2.65
GCI^{12}	0.079	0.016
GCI^{23}	0.129	0.040
Asymptotic convergence level, $GCI^{23} / (r^p * GCI^{12})$	1.04	1.02

variation of the cell sizes and time step in Tables 11 and 12. This indicates that with the applied cell sizes and time steps the discretisation uncertainty is dominated by the influence of the spatial discretisations.

The sensor and DAQ uncertainties were described in Section 2 and could be applied to the measurement results. The repeatability was analysed by Tödter et al. [6]. Thus, repeatability and uncertainties could be combined to quantify the reliability of the experiments. Uncertainties and repeatability (mean value and standard deviation) were summarised in Table 13 for selected sensors. Recall, for example, that the pressure measurement uncertainty consisted of 1% of the full-scale measurement range, 1.7 bar, 0.1% calibration uncertainty, and 0.05% DAQ uncertainty. The uncertainties were combined linearly to obtain the maximum possible error. To evaluate the velocity uncertainty, it must be taken into account that the test body's position was derived versus time to calculate the velocity. Thus, the velocity uncertainty was twice the added sensor and DAQ uncertainty. Uncertainties of time logging were neglected.

Table 13 shows that the sensor errors for force, strain, and velocity are small compared to the repeatability. Thus, the standard deviation of the repetitions was not a consequence of the sensor uncertainties. Slamming loads are highly nonlinear and extremely sensitive. Slight changes in velocity and small bubbles distribution in the liquid phase led to significant changes in the pressure peak. For the structural integrity, the pressure peak is not relevant due to its short impact duration. The repeatability of the measurements for the forces is decisive. The standard deviation listed in Table 13 can be considered as very small. Note that the experiments were repeated 30 times.

The procedures that may be used for validation and to estimate model errors are reported by e.g., Coleman and Stern [101], AIAA [102], ITTC [103] and ASME [83]. In 2008, Oberkampf and Trucano [104] reviewed Validation and Verification (V&V) techniques and summarised that the methods must be improved. The posterior published method ASME V&V 20 [83] gives the current standard technique for V&V. This paper applies this method using experimental and numerical uncertainties to assess the model error. Firstly, the absolute and percentage comparison error E is determined using the simulated peak value S and the experimental mean result D.

$$E = S - D. \tag{9}$$

$$|E|_{\%} = \frac{|S - D|}{D} \cdot 100\ \% . \tag{10}$$

The validation uncertainty u_V is the root-sum-square of the experimental uncertainty u_D, the numerical uncertainty u_{num}, and the input uncertainty of the simulation u_{input}:

$$u_V^2 = u_D^2 + u_{num}^2 + u_{input}^2 . \tag{11}$$

The corresponding expanded uncertainties are calculated as

$$U_i = k \cdot u_i , \tag{12}$$

where i represents V, D, num, $input$ respectively as in Eq. (11) and k is the expansion factor. The errors are assumed to be normally distributed and therefore $k = 2$ is chosen for 95% confidence [83]. The experimental uncertainty u_D was quantified according to Table 13. Here, the uncertainties contain calibration, sensor and data acquisition uncertainties as well as the standard deviation of the repetitions interpreted as percentage uncertainty. The numerical uncertainty u_{num} was calculated following ASME V&V [83] as

$$u_{num} = \frac{\mathrm{GCI}^{12}}{k} , \tag{13}$$

where the representative GCI^{12} was calculated based on peak values of solution variables yielding $u_{num} = 7.62\%$ for force and $u_{num} = 7.57\%$ for pressure at P1 separately for rigid impact simulations; and yielding $u_{num} = 0.72\%$ for force, $u_{num} = 0.49\%$ for pressure at P1,

Table 13
Uncertainty parameters of selected sensors for experimental hydroelastic impact at 0.782 m/s impact velocity.

Sensor	Mean Value $\bar{x}$	Sensor and DAQ Errors	Standard Deviation
P1	25.510 kPa	1.7 kPa + 0.15% $\cdot \bar{x} = 1.738$ kPa	2.280 kPa
F	1.500 kN	0.07% $\cdot \bar{x} = 1.050 \cdot 10^{-3}$kN	0.028 kN
S1	1.919 mm/m	0.13% $\cdot \bar{x} = 2.495 \cdot 10^{-3}$mm/m	0.095 mm/m
Velocity	0.782 m/s	0.10% $\cdot \bar{x} = 7.820 \cdot 10^{-4}$m/s	0.012 m/s

$u_{num} = 2.60\%$ for strain at S1 and $u_{num} = 2.71\%$ for strain at S2 respectively for hydroelastic impact simulations using FFSI. For the input uncertainty u_{input} only the contribution from the uncertainty of the impact velocity is considered. Sensitivity coefficient method [83] was used, where a second order polynomial was fit into the simulation data with different velocities for the evaluation of the corresponding sensitivity derivatives.

Then, the interval containing model error δ_{model} with a confidence level of 95% for a validation variable at specified conditions is represented as

$$E - U_V \leq \delta_{\text{model}} \leq E + U_V \,. \tag{14}$$

To further interpret the results, Eça et al. [105] and Roache [106] classified four different groups to explain the model error δ_{model} based on Eq. (14):

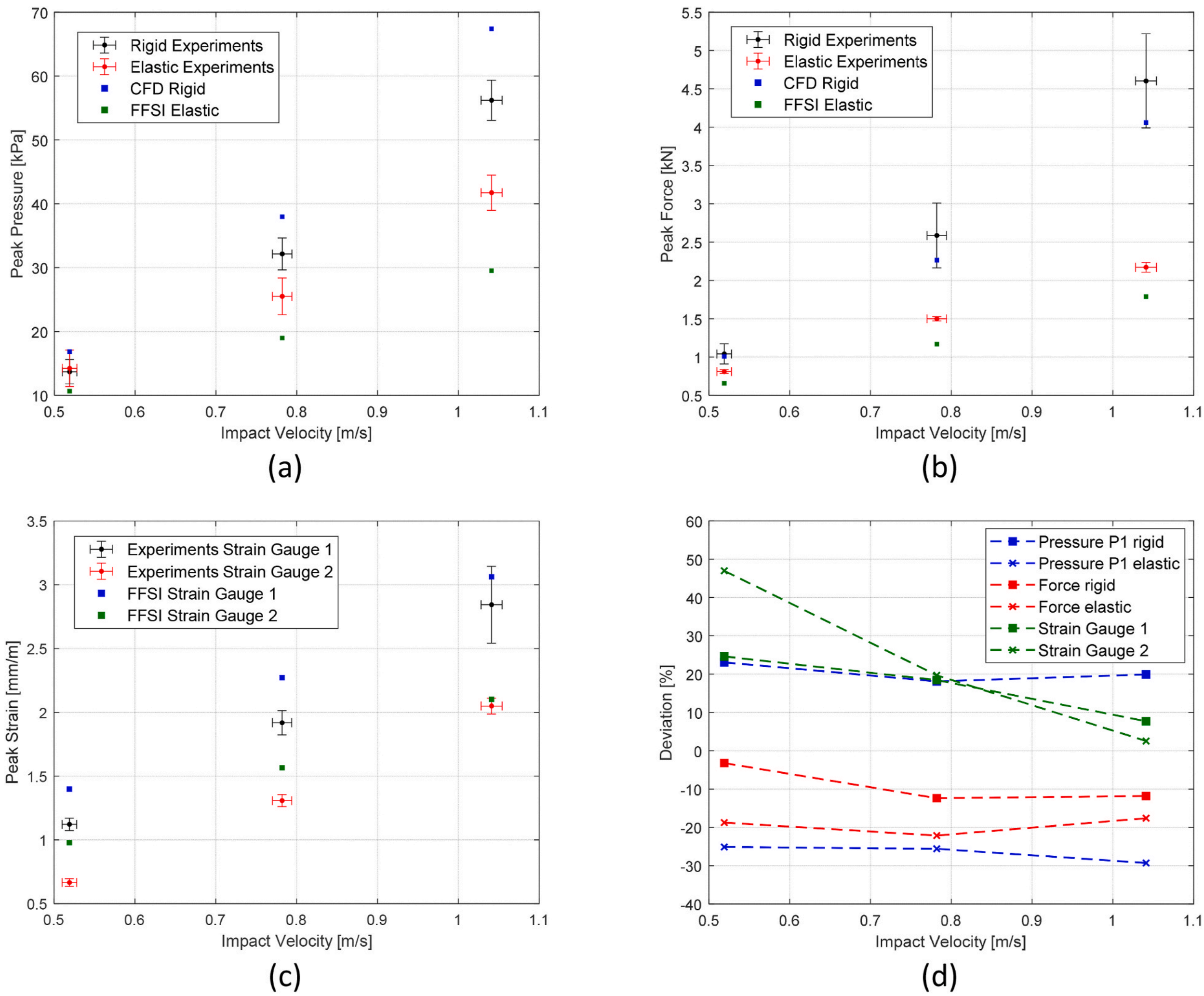

Fig. 14. Numerical peak values and experimental mean peak values of pressure sensor P1 (a), force sensor (b) and strain gauge 1 (c) with associated uncertainties due to sensor and DAQ accuracy and repeatability, and percentage deviations between experimental mean peak values and numerical peak values (d) for the pressures at sensor P1, forces, and strains.

1. $|E| \gg U_V$: $\delta_{\text{model}} \approx E$.
2. $|E| \ll U_V$: $|\delta_{\text{model}}| \leq U_V$ where the sign of the model error is not identified.
3. $|E| \geq U_V$: $|\delta_{\text{model}}| < |E| + U_V$ where the sign of δ_{model} is equal to the sign of E.
4. $|E| < U_V$: $|\delta_{\text{model}}| < |E| + U_V$ where the sign of δ_{model} is unknown.

To further justify the classes of model error for a validation variable, the conditions fulfilling $'\ll'$ and $'\gg'$ must be quantified. Eça et al. [105] proposed the conditions $|E| > C \cdot U_V$, $U_V/C \geq |E|$, $C \cdot U_V \geq |E| \geq U_V$, and $U_V \geq |E| \geq U_V/C$ for the classes one to four, respectively. According to Eça et al. [105], $C = 7$ is suitable for most applications which is also applied for the following comparison.

Fig. 14(a–c) shows experimental mean peak pressures of pressure sensor P1, the mean peak forces and mean peak strains of S1 and S2 with associated uncertainties due to sensor and DAQ accuracy and repeatability, where the numerical peak values were pictured together. The velocity uncertainty was also depicted. Fig. 14(d) depicts the percentage deviation between simulated peak values and experimental mean peak values. The deviation represents the comparison error calculated by Eq. (10) including the sign of the deviation. Generally, the deviation of peak forces was relatively small as forces derived from pressure integration were not prone to spatial fluctuations. However, spatial fluctuations might contribute to the higher deviations for local peak strains and pressures. As mentioned above pressure peak is very sensitive to flow properties during impact. Also note that the numerical impact velocities were perfectly constant whereas there were some small fluctuations of experimental impact velocities, which made the velocities not ideally identical. This difference may partially explain the deviation. Another important aspect to consider for the deviations in Fig. 14 was the numerical modelling uncertainty as mentioned at the front part of this section and in Section 3.2. The peak values may be significantly influenced by high frequency vibration modes, which was under influence of e.g., boundary conditions. The results were also sensitive to the modelling details. For example, there may be overestimation of peak pressures for rigid case as the numerical model was completely rigid but experimental setup was slightly flexible. And underestimation of peak pressures but overestimation of deformation with the elastic plate case may be closely related to the local flexibility modelling. However, it is not practically possible to exactly model all the details of the experimental boundary conditions in the simulations.

Table 14 lists the absolute and percentage comparison Error E, the expanded uncertainties U_{input}, U_D and U_V with a confidence level of 95%, the classification of the validation as well as the interval of the model error δ_{model} for rigid peak forces and pressures. It is always $E > 0$ for pressures and $E < 0$ for forces, indicating that the simulations overpredict peak pressures and underpredict peak forces, which agrees discussions in section 4.1 and observation of Fig. 14. The percentage comparison Errors $|E|_{\%}$ of peak forces are generally smaller than those of peak pressures, which again may be due to the different influences of spatial fluctuations. Comparing expanded validation uncertainties U_V, U_V of peak pressures at P1 decrease with increasing impact velocity and U_V of peak forces are generally larger than those of peak pressures. U_V is dominated by experimental U_D which is dominated by the standard deviation of the repetitions and, thus, by the repeatability of the experiments. Therefore, forces may be more sensitive to the differences between repeated experiments, e.g., small impact angle variation between calm water surface and experimental device with rigid impacts.

Table 15 lists the absolute and percentage comparison Error E, the expanded uncertainties U_{input}, U_D and U_V with a confidence level of 95%, the classification of the validation as well as the interval of the model error δ_{model} for hydroelastic peak forces, pressure and strains. It is always $E < 0$ for forces and pressures and $E > 0$ for strains, i.e., the simulated peak forces and pressures are underpredicted while peak strains are overpredicted, which is in line with the observations in section 4.2 and Fig. 14. Like rigid impact, U_V of peak pressures at P1 decrease with increasing impact velocity. However, both U_V and U_D of peak forces are smaller than those of pressures. This may indicate that peak forces in hydroelastic impact are more consistent and less sensitive than in rigid impact. In addition, the experimental uncertainty U_D is significantly larger for peak pressures compared to peak forces and strains. This may be due to the spatial bubble distributions and high vibration modes being more stochastic leading to large spatial variations in experiments.

Considering the above for both rigid and elastic hydroelastic impacts, the corresponding findings regarding validation and uncertainty are as follows. 1) As U_V is generally dominated by experimental U_D where U_{input} and U_{num} are relatively small, and U_D is generally dominated by repeatability uncertainty, careful experimental repetition study is highly important for validation in study of local slamming problems considering its stochastic features. 2) Wang et al. [61] showed that parameter-based discretisation study is necessary. This paper further indicates that validation uncertainty is also parameter specific, e.g., the force and pressure have different validation uncertainty features with significantly different experimental uncertainties; 3) Generally, the percentage validation uncertainty tends to be clearly smaller for higher speeds of impact for pressure and roughly constant for force. In addition, this paper highlights the difficulties associated with validation of hydroelastic simulation models and highlights importance of well documented experiments for validation.

Table 14
Comparison errors E, expanded input uncertainties U_{input}, expanded experimental uncertainties U_D, expanded validation uncertainties U_V, validation classification, and interval of model error δ_{model} of peak values for rigid impact simulations using CFD.

	Velocity [m/s]	E	$\lvert E\rvert_{\%}$ [%]	U_{input} [%]	U_D [%]	U_V [%]	δ_{model} [%]	Class
Force	0.519	−0.03 kN	3.21	6.81	25.17	30.20	[-33.41, 26.99]	2
	0.782	−0.32 kN	12.38	5.56	32.71	36.52	[-48.90, 24.14]	4
	1.041	−0.54 kN	11.81	4.54	26.64	31.02	[-42.83, 19.21]	4
Pressure P1	0.519	3.16 kPa	23.06	8.74	28.02	33.02	[-9.96, 56.08]	4
	0.782	5.82 kPa	18.10	7.50	15.61	23.00	[-4.90, 41.10]	4
	1.041	11.19 kPa	19.91	6.19	11.16	19.80	[0.11, 39.71]	3

Table 15
Comparison errors E, expanded input uncertainties U_{input}, expanded experimental uncertainties U_D, expanded validation uncertainties U_V, validation classification, and interval of model error δ_{model} of peak values for hydroelastic impact simulations using FFSI.

	Velocity [m/s]	E	$\lvert E\rvert_{\%}$ [%]	U_{input} [%]	U_D [%]	U_V [%]	δ_{model} [%]	Class
Force	0.519	−0.15 kN	18.75	3.79	6.17	7.38	[-26.14, −11.37]	3
	0.782	−0.33 kN	22.12	3.48	3.74	5.30	[-27.42, −16.82]	3
	1.041	−0.38 kN	17.61	3.15	5.81	6.76	[-24.37, −10.85]	3
Pressure P1	0.519	−3.57 kPa	25.10	3.43	40.01	40.17	[-65.27, 15.07]	4
	0.782	−6.53 kPa	25.59	3.41	22.48	22.76	[-48.34, −2.83]	3
	1.041	−12.22 kPa	29.28	2.82	13.21	13.54	[-42.82, −15.74]	3
Strain S1	0.519	0.28 mm/m	24.62	5.57	8.56	11.46	[13.15, 36.08]	3
	0.782	0.35 mm/m	18.44	3.99	9.90	11.88	[6.55, 30.32]	3
	1.041	0.22 mm/m	7.71	2.67	21.17	21.96	[-14.26, 29.67]	4
Strain S2	0.519	0.31 mm/m	46.97	6.25	9.01	12.24	[34.73, 59.20]	3
	0.782	0.26 mm/m	19.69	3.96	7.19	9.84	[9.85, 29.52]	3
	1.041	0.05 mm/m	2.56	2.54	6.05	8.51	[-5.95, 11.08]	4

In addition, it should be noted that the paper compares simulations and experiments for the case of an unstiffened plate structure subject to different impact velocities to a maximum up to about 1 m/s. This is mainly because of results made available following pre-existing experiments and limitations in the maximum loading capacity of the available test-rig. FFSI simulations demonstrated that structural flexibility and air gap effects are important in terms of quantifying the response. Yet the specific influence of damping on hydroelasticity and direct application of the method on stiffened plate structures will be the subject matter of future research.

6. Conclusions

Numerical simulations of flat plate impacts were carried out to analyse the capability of the applied methods. Computational Fluid Mechanics (CFD) was used to model rigid impacts. Two-way coupled Flexible Fluid-Structure Interaction (FFSI), using ABAQUS for the structural domain and STAR CCM + for the fluid domain, was applied for hydroelastic water impacts. The modelled test bodies had the same dimensions and properties as those experimentally investigated by Tödter et al. [6].

For rigid impacts, time histories of simulations and experiments attained similar peak loads. For hydroelastic impacts, the two-way FFSI coupling method presented was able to reasonably idealize the influence of modal actions and air entrapment on response. The numerically obtained natural frequency of the elastic plate in a vacuum differed only slightly from the experimentally assessed natural frequency in air. Simulated time histories correlated favourably with a series of thirty repetitive experimental measurements of peak loads and load oscillations after the peak. The simulated void fraction underneath the impacting plates compared favourably to cavities experimentally captured by high-speed imaging.

Uncertainties of the simulations and the experiments were assessed to increase the significance of the validation. Specifically, not only the accuracies of sensors and the data acquisition system were assessed, but also the associated uncertainties of the repetitive experimental results. The discretisation uncertainties were quantified using the Grid Convergence Index (GCI) methods. The uncertainty range of peak pressures, forces and strains clarified the differences between numerically and experimentally obtained results. Here, differences were the smallest for forces because they were not influenced by local effects. Pressures and strains were prone to spatial effects, which led to deviations between experiments and simulations. Additionally, simulated peak loads may have been affected by high frequency vibration modes and their interaction with boundary conditions, as these were sensitive to modelling details.

In addition, the American society of Mechanical Engineers (ASME) standard for Verification and Validation (V&V) [83] is used to estimate the errors of experiments and simulations. The corresponding findings are 1) careful experimental study with large number of repetitions is highly important for validation of models for local slamming problems considering its stochastic features; 2) validation uncertainty is also parameter specific; 3) the percentage validation uncertainty tends to be smaller for higher speeds of impact in case of pressure and roughly independent of the velocity in case of force. Well documented experiments and close co-operation between experimentalist and simulation engineers for validation are highly recommended.

Declaration of competing interest

The authors declare that they have no known competing financial interests or personal relationships that could have appeared to influence the work reported in this paper.

References

[1] von Kármán T. The impact on seaplane floats during landing. National Advisory Committee for Aeronautics - Technical Notes; 1929. p. 321.
[2] Wagner H. Über Stoß- und Gleitvorgänge an der Oberflache von Flüssigkeiten. Z Angew Math Mech 1932;12:193–215.
[3] Chuang S-L. Slamming of rigid wedge-shaped bodies with various deadrise angles. Structural Mechanics Laboratory - Research and Development Report 1966: 2268.
[4] Oh SH, Kwon SH, Chung JY. A close look at air pocket evolution in flat impact. In: Proc. 24th int. Work. Water waves float. Bodies, zel. Russ.; 2009.

[5] Oh SH, Kwon SH, Kwak DW, Choi YM. An attempt to demystify flat impact. In: Proc. 25th int. Work. Water waves float. Bodies. China: Harbin; 2010.
[6] Tödter S, el Moctar O, Neugebauer J, Schellin TE. Experimentally measured hydroelastic effects on impact-induced loads during flat water entry and related uncertainties. J Offshore Mech Arctic Eng 2020;142:011604. https://doi.org/10.1115/1.4044632.
[7] Phi TH, Ahn HT. Air compressibility effect in CFD-based water impact analysis. J Soc Nav Archit Korea 2011;48:581–91.
[8] el Moctar O, Tödter S, Neugebauer J, Schellin TE. Investigation of hydroelasticity and air compressibility on impact loads. In: 8th int. Conf. Hydroelasticity mar. Technol. Seoul; 2018. Korea.
[9] Lewison G, Maclean WM. On the cushioning of water impact by entrapped air. J Ship Res 1968;11:116–30.
[10] Verhagen JHG. The impact of a flat plate on a water surface. J Ship Res 1967;11:211–23.
[11] Chuang S-L. Experiments on flat-bottom slamming. J Ship Res 1966;10:10–7.
[12] Yamamoto Y, Ohtsubo H, Okada S, Sawada M, Murakami T. Cushioning action for horizontal water impact of a flat plate. J Soc Nav Archit Jpn 1983;153: 235–42. https://doi.org/10.1201/9781482267037-259.
[[13] Mayer HC, Krechetnikov R. Flat plate impact on water. J Fluid Mech 2018;850:1066–116. https://doi.org/10.1017/jfm.2018.461.
[14] Smith NJ, Stansby PK, Wright JR. The slam force on a flat plate in free flight due to impact on a wave crest. J Fluid Struct 1998;12:183–96. https://doi.org/10.1006/jfls.1997.0132.
[15] Iwanowski B, Fujikubo M, Yao T. Analysis of horizontal water impact of a rigid body with the air cushion effect. J Soc Nav Archit Jpn 1993;173:293–302. https://doi.org/10.2534/jjasnaoe1968.1993.293.
[16] Iafrati A, Korobkin AA. Initial stage of flat plate impact onto liquid free surface. Phys Fluids 2004;16:2214–27. https://doi.org/10.1063/1.1714667.
[17] Jiang Z, Yang J, Zong M, Xu Y. Air-cushion and impact force coefficient with the water entry of a flat rigid body. Proc. 28th Int. Offshore Polar Eng. Conf. Sapporo, Japan 2018:89–93.
[18] Huera-Huarte FJ, Jeon D, Gharib M. Experimental investigation of water slamming loads on panels. Ocean Eng 2011;38:1347–55. https://doi.org/10.1016/j.oceaneng.2011.06.004.
[19] Bereznitski A. Slamming: the role of hydroelasticity. Int Shipbuild Prog 2001;48:333–51.
[20] Faltinsen OM. Hydroelastic slamming. J Mar Sci Technol 2001;5:49–65. https://doi.org/10.1007/s007730070011.
[21] Mäkiharju SA, Elbing BR, Wiggins A, Schinasi S, Vanden-Broeck J-M, Perlin M, et al. On the scaling of air entrainment from a ventilated partial cavity. J Fluid Mech 2013;732:47–76. https://doi.org/10.1017/jfm.2013.387.
[22] Young YL, Harwood CM, Miguel Montero F, Ward JC, Ceccio SL. Ventilation of lifting bodies: review of the physics and discussion of scaling effects. Appl Mech Rev 2017;69:10801. https://doi.org/10.1115/1.4035360.
[23] Faltinsen OM. The effect of hydroelasticity on ship slamming. Philos Trans R Soc A Math Phys Eng Sci 1997;355:575–91. https://doi.org/10.1098/rsta.1997.0026.
[24] Kapsenberg GK. Slamming of ships: where are we now? Phil. Trans. R. Soc. A. 2011;369:2892–919. https://doi.org/10.1098/rsta.2011.0118.
[25] Dias F, Ghidaglia JM. Slamming: recent progress in the evaluation of impact pressures. Annu Rev Fluid Mech 2018;50:243–73. https://doi.org/10.1146/annurev-fluid-010816.
[26] Wang S, Guedes Soares C. Review of ship slamming loads and responses. J Mar Sci Appl 2017;16:427–45. https://doi.org/10.1007/s11804-017-1437-3.
[27] Xu GD, Duan WY. Review of prediction techniques on hydrodynamic impact of ships. J Mar Sci Appl 2009;8:204–10. https://doi.org/10.1007/s11804-009-8039-7.
[28] Truong DD, Jang BS, Janson CE, Ringsberg JW, Yamada Y, Takamoto K, et al. Benchmark study on slamming response of flat-stiffened plates considering fluid-structure interaction. Mar Struct 2021:79.
[29] Tenzer M, el Moctar O, Schellin TE. Experimental investigation of impact loads during water entry. Ship Technol Res 2015;62:47–59. https://doi.org/10.1179/0937725515Z.0000000003.
[30] Panciroli R, Abrate S, Minak G. Dynamic response of flexible wedges entering the water. Compos Struct 2013;99:163–71. https://doi.org/10.1016/j.compstruct.2012.11.042.
[31] Panciroli R, Abrate S, Minak G, Zucchelli A. Hydroelasticity in water-entry problems: comparison between experimental and SPH results. Compos Struct 2012; 94:532–9. https://doi.org/10.1016/j.compstruct.2011.08.016.
[32] Ren Z, Javaherian MJ, Gilbert CM. Kinematic and inertial hydroelastic effects caused by vertical slamming of a flexible V-shaped wedge. J Fluid Struct 2021; 103:103257. https://doi.org/10.1016/j.jfluidstructs.2021.103257.
[33] Ren Z, Wang Z, Stern F, Judge C, Ikeda-Gilbert C. Vertical water entry of a flexible wedge into calm water: a fluid–structure interaction experiment. J Ship Res 2019;63:41–55. https://doi.org/10.5957/JOSR.09180087.
[34] Luo H, Wang H, Guedes Soares C. Numerical and experimental study of hydrodynamic impact and elastic response of one free-drop wedge with stiffened panels. Ocean Eng 2012;40:1–14. https://doi.org/10.1016/j.oceaneng.2011.11.004.
[35] Carcaterra A, Ciappi E. Hydrodynamic shock of elastic structures impacting on the water: theory and experiments. J Sound Vib 2004;271:411–39. https://doi.org/10.1016/j.jsv.2003.02.005.
[36] Stenius I, Rosén A, Battley M, Allen T. Experimental hydroelastic characterization of slamming loaded marine panels. Ocean Eng 2013;74:1–15. https://doi.org/10.1016/j.oceaneng.2013.09.007.
[37] Okada S, Sumi Y. On the water impact and elastic response of a flat plate at small impact angles. J Mar Sci Technol 2000;5:31–9. https://doi.org/10.1007/s007730070019.
[38] Mai T, Mai C, Raby A, Greaves DM. Hydroelasticity effects on water-structure impacts. Exp Fluid 2020;61:191. https://doi.org/10.1007/s00348-020-03024-3.
[39] Yan F, Zhang C, Sun L, Zhang D. Experimental study on slamming pressure and hydroelastic vibration of a flat plate during water entry. J Coast Res 2015;73: 594–9. https://doi.org/10.2112/SI1-103.1.
[40] Yan F, Ma Q, Sun L. On slamming pressure of flat elastic plates with different aspect ratios. Coast Eng J 2016;58:1650015. https://doi.org/10.1142/S0578563416500157.
[41] Shin H, Seo B, Cho SR. Experimental investigation of slamming impact acted on flat bottom bodies and cumulative damage. Int J Nav Archit Ocean Eng 2018; 10:294–306. https://doi.org/10.1016/j.ijnaoe.2017.06.004.
[42] Zhu L, Duan L, Chen M, Yu TX, Pedersen PT. Equivalent design pressure for ship plates subjected to moving slamming impact loads. Mar Struct 2020;71. https://doi.org/10.1016/j.marstruc.2020.102741.
[43] Kvalsvold J, Faltinsen OM. Hydroelastic modelling of slamming against the wetdeck of a catamaran. In: Pro second int conf Fast sea transportation; 1993. p. 681–97. Fast'93, Japan.
[44] Kvalsvold J, Faltinsen OM. Slamming loads on wetdecks of multihull vessels. In: Pro second int conf hydroelasticity in marine technology; 1994. p. 205–20. Trondheim, Norway.
[45] Kvalsvold J, Faltinsen OM. Hydroelastic modelling of wetdeck slamming on multihull vessels. J Ship Res 1995;39:225–39.
[46] Faltinsen OM, Kvalsvold J, Aarsnes JV. Water impact on a horizontal elastic plate. J Mar Sci Technol 1997;2:87–100.
[47] Korobkin AA. Wave impact on the center of an Euler beam. J Appl Mech Tech Phys 1998;39(5):770–81.
[48] Khabakhpasheva TI. Impact of a surface wave on an elastic hull. Fluid Dynam 2006;41(3):424–33.
[49] Korobkin AA, Gueret R, Malenica S. Hydroelastic coupling of beam finite element model with Wagner theory of water impact. J Fluid Struct 2006;22:493–504.
[50] Khabakhpasheva TI, Korobkin AA. Elastic wedge impact onto a liquid surface: wagner's solution and approximate models. J Fluid Struct 2013;36:32–49.
[51] Wang S, Karmakar D, Guedes Soares C. Hydroelastic impact of a horizontal floating plate with forward speed. J Fluid Struct 2016;60:97–113. https://doi.org/10.1016/j.jfluidstructs.2015.11.005.
[52] Lv J, Grenestedt JL. Analytical study of the responses of bottom panels to slamming loads. Ocean Eng 2015;94:116–25.
[53] Wang S, Guedes Soares C. Numerical study on hydroelastic water entry of a wedge. Dev Marit Transp Exploit Sea Resour 2014;1:199–205. https://doi.org/10.1201/b15813-26.

[54] Andrun M, Bašić J, Blagojević B, Klarin B. Simulating hydroelastic slamming by coupled Lagrangian-fdm and FEM. Prog Mar Sci Technol 2020;5:135–42. https://doi.org/10.3233/PMST200036.
[55] Aghaei A, Schimmels S, Schlurmann T, Hildebrandt A. Numerical investigation of the effect of aeration and hydroelasticity on impact loading and structural response for elastic plates during water entry. Ocean Eng 2020;201:107098. https://doi.org/10.1016/j.oceaneng.2020.107098.
[56] Truong DD, Jang BS, Ju HB, Han SW. Prediction of slamming pressure considering fluid-structure interaction. Part I: numerical simulations. Ships Offshore Struct 2020:1–22. https://doi.org/10.1080/17445302.2020.1816732.
[57] Truong DD, Jang BS, Ju HB, Han SW. Prediction of slamming pressure considering fluid-structure interaction. Part II: derivation of empirical formulations. Mar Struct 2021;75:102700. https://doi.org/10.1016/j.marstruc.2019.102700.
[58] Wang H, Cheng Y, Liu J, Zhang P. Thin-Walled Structures Hydroelastic behaviours of laser-welded lightweight corrugated sandwich panels subjected to water impact : experiments and simulations. Thin-Walled Struct 2020;146:106452. https://doi.org/10.1016/j.tws.2019.106452.
[59] Liao K, Hu C, Sueyoshi M. Numerical simulation of free surface flow impacting on an elastic plate. In: Proc. 29th int. Work. Water waves float. Bodies; 2014. Osaka, Japan.
[60] Liao K, Hu C, Sueyoshi M. Free surface flow impacting on an elastic structure: experiment versus numerical simulation. Appl Ocean Res 2015;50:192–208. https://doi.org/10.1016/j.apor.2015.02.002.
[61] Wang S, Islam H, Guedes Soares C. Uncertainty due to discretization on the ALE algorithm for predicting water slamming loads. Mar Struct 2021;80:103086. https://doi.org/10.1016/j.marstruc.2021.103086.
[62] Shams A, Porfiri M. Treatment of hydroelastic impact of flexible wedges. J Fluid Struct 2015;57:229–46. https://doi.org/10.1016/j.jfluidstructs.2015.06.017.
[63] Shams A, Zhao S, Porfiri M. Analysis of hydroelastic slamming of fexible structures: modeling and experiments. Procedia Eng 2017;199:1484–8. https://doi.org/10.1016/j.proeng.2017.09.422.
[64] Lv J, Grenestedt JL. Some analytical results for the initial phase of bottom slamming. Mar Struct 2013;34:88–104. https://doi.org/10.1016/j.marstruc.2013.08.004.
[65] Panciroli R, Abrate S, Minak G, Zucchelli A. Hydroelasticity in water-entry problems: comparison between experimental and SPH results. Compos Struct 2012;94:532–9. https://doi.org/10.1016/j.compstruct.2011.08.016.
[66] Yang QY, Qiu W. Computation of slamming forces on 3-D bodies with a CIP method. In: 29th int. Conf. Ocean. Offshore arct. Eng. Shanghai. OMAE; 2010. China.
[67] Wang S, Guedes Soares C. Hydroelastic analysis of a rectangular plate subjected to slamming loads. J Mar Sci Appl 2017;16:405–16. https://doi.org/10.1007/s11804-017-1434-6.
[68] Wang S, Karmakar D, Guedes Soares C. Hydroelastic impact due to longitudinal compression on transient vibration of a horizontal elastic plate. Marit Technol Eng 2015;2:1073–9. https://doi.org/10.1201/b17494-144.
[69] Antoci C, Gallati M, Sibilla S. Numerical simulation of fluid – structure interaction by SPH. Comput Struct 2007;85:879–90. https://doi.org/10.1016/j.compstruc.2007.01.002.
[70] Yang Q, Xu F, Yang Y, Wang J. Two-phase SPH model based on an improved Riemann solver for water entry problems. Ocean Eng 2020;199:107039. https://doi.org/10.1016/j.oceaneng.2020.107039.
[71] Khayyer A, Gotoh H, Falahaty H, Shimizu Y, Nishijima Y. Towards development of a reliable fully-Lagrangian MPS-based FSI solver for simulation of 2D hydroelastic slamming. Ocean Syst Eng 2017;7:299–318. https://doi.org/10.12989/ose.2017.7.3.299.
[72] Khayyer A, Shimizu Y, Gotoh H, Hattori S. Multi-resolution ISPH-SPH for accurate and efficient simulation of hydroelastic fluid-structure interactions in ocean engineering. Ocean Eng 2021;226:108652. https://doi.org/10.1016/j.oceaneng.2021.108652.
[73] Allen T. Mechanics of flexible composite hull panels subjected to water impacts. New Zealand: The University of Auckland; 2013.
[74] Scolan YM. Hydroelastic behaviour of a conical shell impacting on a quiescent-free surface of an incompressible liquid. J Sound Vib 2004;277:163–203. https://doi.org/10.1016/j.jsv.2003.08.051.
[75] Oger G, Guilcher P, Jacquin E, Brosset L, Deuff JB, Le Touzé D. Simulations of hydro-elastic impacts using a parallel SPH model. Int J Offshore Polar Eng 2010;20.
[76] Sun Z, Zhang GY, Zong Z, Djidjeli K, Xing JT. Numerical analysis of violent hydroelastic problems based on a mixed MPS- mode superposition method. Ocean Eng 2019;179:285–97. https://doi.org/10.1016/j.oceaneng.2019.03.032.
[77] Southall N, Choi S, Lee Y, Hong C, Hirdaris S, White N. Impact analysis using CFD–a comparative study. Hawaii, USA. In: Proceedings of the 25th international ocean and polar engineering conference, kona, big island. ISOPE; 2015. June 21-26, ISOPE '15, ISBN 978-1-880653-89-0.
[78] Maki KJ, Lee D, Troesch AW, Vlahopoulos N. Hydroelastic impact of a wedge-shaped body. Ocean Eng 2011;38:621–9. https://doi.org/10.1016/j.oceaneng.2010.12.011.
[79] Maki KJ, Lee D, Troesch AW, Vlahopoulos N. Hydroelastic impact of a wedge-shaped body. Ocean Eng 2011;38:621–9. https://doi.org/10.1016/j.oceaneng.2010.12.011.
[80] Ren Z, Wang Z, Stern F, Judge C, Ikeda-Gilbert C. Vertical water entry of a flexible wedge into calm water: a fluid–structure interaction experiment. J Ship Res 2019;63:41–55. https://doi.org/10.5957/JOSR.09180087.
[81] Lakshmynarayanana PAK, Hirdaris S. Comparison of nonlinear one- and two-way FFSI methods for the prediction of the symmetric response of a containership in waves. Ocean Eng 2020;203:107179. https://doi.org/10.1016/j.oceaneng.2020.107179.
[82] Yan D, Hosseinzadeh S, Lakshmynarayanana A, Mikkola T, Hirdaris S. Comparative study on numerical hydroelastic analysis of impact-induced loads. In: Proceedings of the 23rd numerical towing tank symposium. NuTTs; 2021 (Nutts 2021), p.6, https://www.uni-due.de/ISMT/ismt_nutts_2021.php.
[83] ASME. Standard for verification and validation in computational fluid dynamics and heat transfer: ASME V&V 20. American Society of Mechanical Engineers; 2009.
[84] Ferziger JH, Peric M. Computational methods for fluid dynamicsvol. 3. Berlin: Springer; 2002.
[85] STAR CCM+. User manual for STAR CCM+. Florida, USA: Sabalcore; 2018.
[86] Reddy DN, Scanlon T, Kuo K. Prediction of slam loads on wedge section using computational fluid dynamics (CFD) techniques. In: 24th symp. Nav. Hydrodyn.; 2002. p. 708–20. Fukuoka, Japan.
[87] Southall NR, Lee Y, Johnson MC, Hirdaris SE, White NJ. Towards a pragmatic method for prediction of whipping: wedge impact simulations using OpenFOAM. Proc Int Offshore Polar Eng Conf 2014;3:806–15.
[88] Hirt CW, Nichols BD. Volume of fluid (VOF) method for the dynamics of free boundaries. J Comput Phys 1981;39:201–25.
[89] Dassault Systèmes. Abaqus theory guide. 2016. Providence, Rhode Island, U.S.A.
[90] Lakshmynarayanana P. Application of 3-D CFD modelling to predict the dynamic behaviour of Ship in waves. University of Southampton; 2017.
[91] Camilleri J. Experimental and numerical investigation of slamming loads on high-speed craft including hydroelastic effects. University of Southampton; 2017.
[92] Muzaferija S, Peric M, Sames P, Schellin TE. A two-fluid Navier-strokes solver to simulate water entry. In: 22nd symp. Nav. Hydrodyn.; 1998. p. 277–89. Washington D.C., U.S.A.
[93] ASME. Procedure for estimation and reporting of uncertainty due to discretization in CFD applications. J Fluid Eng 2008;130. https://doi.org/10.1115/1.2960953. 078001-1-078001–4.
[94] Stern F, Wilson RV, Coleman HW, Paterson EG. Comprehensive approach to verification and validation of CFD simulations—Part 1: methodology and procedures. J Fluids Eng Trans ASME 2001;123:793–802. https://doi.org/10.1115/1.1412235.
[95] Xiao J, Batra RC. Delamination in sandwich panels due to local water slamming loads. J Fluid Struct 2014;48:122–55. https://doi.org/10.1016/j.jfluidstructs.2014.02.008.
[96] Smith RR, McCrary SW, Callahan RN. Gauge repeatability and reproducibility studies and measurement system analysis: a multimethod exploration of the state of practice. J Ind Technol 2007;23:1–12.
[97] Xing T, Stern F. Factors of safety for Richardson extrapolation. J. Fluids Eng., Trans. ASME 2010;132(6):0614031–40313.

[98] Huang S, Jiao J, Guedes Soares C. Uncertainty analyses on the CFD–FEA co-simulations of ship wave loads and whipping responses. Mar. Struct. 2022;82.
[99] Celik IB, Ghia U, Roache PJ, Freitas CJ, Coleman H, Raad PE. Procedure for estimation and reporting of uncertainty due to discretization in CFD applications. J. Fluids Eng. Trans. ASME 2008;130. https://doi.org/10.1115/1.2960953. 0780011–0780014.
[100] Roache PJ. Verification and validation in computational science and engineering. Albuquerque, New Mexico: Hermosa Publishers; 1998.
[101] Coleman HW, Stern F. Uncertainties and CFD code validation. J Fluid Eng 1998;119:795–803.
[102] AIAA. Guide for the verification and validation of computational fluid dynamics simulations. American Institute of Aeronautics and Astronautics; 1998. AIAA-G-077.
[103] ITTC. Uncertainty analysis in CFD Verification and validation methodology and procedures. ITTC - Recommended Procedures and Guidelines 2017. Procedure 7.5-03-01, pp.1–13, https://www.ittc.info/media/8153/75-03-01-01.pdf.
[104] Oberkampf WL, Trucano TG. Verification and validation benchmarks. Nucl Eng Des 2008;238:716–43. https://doi.org/10.1016/j.nucengdes.2007.02.032.
[105] Eca L, Dowding K, Roache PJ. On the interpretation and scope of the V&V 20 standard for verification and validation in computational fluid dynamics and heat transfer. In: Proceedings of the ASME 2020 verification and validation symposium; 2020. V001T02A001.
[106] Roache PJ. Interpretation of validation results following ASME V&V20-2009. J. Verif. Valid. Uncertain. Quantif. 2017;2:2–5. https://doi.org/10.1115/1.4037706.